Ultra-Tightly Coupled GNSS/INS/Vision Integrated System for Centimeter-Level Vehicle Positioning in Challenging Environments

Xin Feng, Tisheng Zhang, *Member, IEEE*, Liqiang Wang, *Graduate Student Member, IEEE*, Xiaoji Niu, *Member, IEEE*, Mohamed Bochkati, Thomas Pany, *Senior Member, IEEE*, and Jingnan Liu

***Abstract*—High-precision positioning plays a pivotal role in intelligent transportation systems by enabling reliable navigation, automated intersection management and high-precision platooning for autonomous vehicles in large-scale, unfamiliar environments. However, existing loosely or tightly coupled integration solutions of Global Navigation Satellite System (GNSS), Inertial Navigation System (INS), and Visual System can be challenged by the limited availability of GNSS signals, which will affect their ability to consistently achieve robust high-precision positioning in harsh environments. In this work, we propose a multi-sensor (GNSS/INS/Vision) ultra-tightly coupled system with GNSS carrier phase long coherent integration tracking (MUT-LCI). At the signal processing level, MUT-LCI utilizes the multi-sensor sensed dynamics to assist GNSS signal tracking loops and realizes extended coherent integration periods up to 300 milliseconds, improving the availability of GNSS carrier phase observations in highly challenging environments significantly. The data fusion of the GNSS RTK/INS/Vision is conducted using a Multi-state Constraint Kalman Filter (MSCKF). To evaluate the performance of the proposed MUT-LCI system, we conducted experiments using an intelligent transportation wheeled robot platform in harsh environments, including areas covered by dense tree canopies and surrounded by tall buildings. The results demonstrate that the proposed MUT-LCI system achieves precise GNSS carrier phase signal tracking in highly challenging environments, enabling continuous RTK fixed solutions and providing reliable centimeter-level positioning accuracy.**

***Index Terms*—GNSS signal tracking loop, GNSS carrier phase, ultra-tight integration, long coherent integration, GNSS/INS/vision.**

I. Introduction

INTELLIGENT Transportation Systems (ITS) rely on Vehicle-to-Vehicle (V2V) and Vehicle-to-Infrastructure (V2I) communication to enable applications such as automated intersection management and high-precision platooning. These applications require autonomous vehicles, such as self-driving cars and smart delivery robots, to accurately determine and share their positions within a global reference coordinate framework [1], [2]. Moreover, achieving high-precision and reliable absolute positioning within a unified coordinate framework is crucial for autonomous vehicles to navigate effectively in large-scale, unknown environments [3], [4]. Global navigation satellite system (GNSS) is hence necessary for its superiority to provide globally-referenced centimeter level positioning (based on carrier phase observations) 24/7 [5]. However, the availability of GNSS precision positioning remains challenging since the GNSS signals will be frequently attenuated, reflected or blocked in harsh environments [6], [7]. Complex signal degradation phenomena lead to tracking errors in GNSS receivers, resulting in large positioning errors [8]. As a result, the utilization of GNSS receivers for autonomous vehicles or smart delivery robots is hindered.

Centimeter level positioning relies on continuous and accurate carrier phase observations, which are generated through continuous tracking of the carrier phase signal by Phase-Locked Loops (PLLs) within the GNSS receiver. PLL is the most fragile part [9]. A tiny signal interference can cause the PLL to lose lock, generating a gross error in the form of undetected cycle slips. In order to provide continuous high precision positioning in harsh environments, both the academic and industrial sectors have proposed numerous solutions.

A large category of solutions focus on data processing, which include high precision GNSS positioning algorithms and integration navigation techniques combining GNSS and other sensors.

Typical centimeter accurate GNSS positioning techniques include Real-Time Kinematic (RTK), Precise Point Positioning (PPP) and PPP-RTK. RTK positioning relies on the accurate observations of a reference station to provide real-time corrections [10]. It is the most widely used techniques in mass-market applications. PPP can provide centimeter positioning accuracy with un-differenced carrier phase observations, but it suffers from extreme long convergence period, which is not suitable for real-time dynamic scenarios [11]. PPP-RTK combines the concepts of RTK and PPP with better performance and flexibility [12]. The rapid development of different GNSS

Received 12 March 2025; revised 27 July 2025 and 5 November 2025; accepted 7 November 2025. Date of publication 19 November 2025; date of current version 18 February 2026. This work was supported in part by the National Natural Science Foundation of China under Grant 42374034 and in part by the Major Program of Hubei Province under Grant 2023BAA02602. The Associate Editor for this article was Z. Xiao. *(Corresponding author: Tisheng Zhang.)*

Xin Feng is with the School of Geodesy and Geomatics, Wuhan University, Wuhan 430079, China.

Tisheng Zhang, Liqiang Wang, Xiaoji Niu, and Jingnan Liu are with the Integrated and Intelligent Navigation (I2Nav) Group, GNSS Research Center, Wuhan University, Wuhan 430072, China (e-mail: zts@whu.edu.cn).

Mohamed Bochkati and Thomas Pany are with the Institute of Space Technology and Space Applications (ISTA), Universitäat der Bundeswehr Müunchen, 85579 Neubiberg, Germany.

Digital Object Identifier 10.1109/TITS.2025.3631873

constellations promote the evolution of these techniques [13]. There are four major GNSS constellations: GPS, BDS, Galileo and GLONASS, providing dozens of available satellites with multiple frequencies [14]. The positioning performance has been significantly enhanced by multi-GNSS positioning. However, standalone multi-GNSS positioning techniques still degrade or even become unavailable when dealing with carrier phase observations in harsh environments [15]. Integrating other sensors for navigation, such as inertial measurement unit (IMU), camera, LiDAR, has become the trend. Related research has been conducted extensively since decades.

The Inertial Navigation System (INS) stands out as the prevalent dead-reckoning navigation system extensively employed for the integration with GNSS [16], [17]. However, since INS error accumulates rapidly with time, the GNSS/INS integration with mass-market grade IMUs still cannot provide positioning service with satisfying accuracy and reliability [18]. With the emergence and rapid development of simultaneous localization and mapping (SLAM) technology, other sensors are extensively studied, with cameras and 3D LiDAR being the most commonly used. A SLAM approach simultaneously estimates the positions of the observed features and the camera/LiDAR itself [19]. If GNSS is not adopted, multi-sensor fusion SLAM approaches with loop-closure detection can realize relative decimeter-level accuracy in restricted areas, which meet the requirements of some small-scale applications, such as sweeping robots. However, navigation in open, large-scale environments may not fulfill the conditions of loop-closure detection, the SLAM system will thus tend to operate as a visual-inertial odometry (VIO), whose error will also accumulate [20]. The hybridization of GNSS and other sensors is required to deliver continuous, accurate and robust absolute positioning.

Data-processing oriented GNSS/INS/Vision or LiDAR integration can be implemented in a loosely or tightly coupled way. Loosely coupled (LC) integration combines the IMU and other sensors' measurements with the position and velocity derived from GNSS [21], [22], [23]. As mentioned before, standalone GNSS receivers produce positions with plenty of gross errors in harsh environments. If not detected, these "poisoned" positions can introduce errors of up to several tens of meters into the system, severely compromising the robustness of the systems.

Instead of using the GNSS receiver as a "black box", tightly coupled multi-sensor integration tend to use it as a "gray box" by processing the raw GNSS observations: pseudo-range, Doppler and carrier phase [24], [25]. Tightly coupled (TC) GNSS/INS/Vision or LiDAR integration fuses the advantages of both the high precision positioning and SLAM techniques, greatly enhancing the accuracy and reliability. In a tightly coupled integration solution, INS typically serves as the core sensor, and the selection of high-precision algorithms (RTK, PPP, PPP-RTK) and other sensors (camera, LiDAR) depends on the specific application scenarios and prospective costs. RTK-based multi-sensor integration first attracted attention due to the maturity of RTK algorithms [26]. Subsequently, the PPP and PPP-RTK based multi-sensor tightly coupled integration techniques were extensively studied in recent years [27], [28]. Related research demonstrates that the ambiguity fixing rate of a high precision algorithm can be improved by multi-sensor integration, resulting in augmented reliability [29]. A state-of-the-art TC GNSS/INS solution [30] explores the use of consumer-grade inertial sensors for tightly coupled urban carrier-phase differential GNSS, providing decimeter level horizontal positioning accuracy. The most advanced study [31] showcases the positioning outcomes of a PPP-RTK/INS/Vision TC architecture, demonstrating decimeter level positioning accuracy and only 68.3% of ambiguity fixing rate in typical urban canyons. Besides, the experiment's challenging scenarios do not encompass long-term satellite signal interference, such as persistent dense foliage. Another work [32] demonstrates the performance of a PPP/INS/Vision/LiDAR tightly coupled integration system under dense foliage around 4 minutes, and only sub-meter level accuracy is achieved. Fundamentally, the LC or TC multi-sensor integration relies on the strong dead-reckoning ability of other non-GNSS sensors to compensate for adverse GNSS measuring conditions. The potential of GNSS is not fully achieved, which prompts researchers to dive into the design of GNSS receivers, improving the availability of GNSS observations through robust signal processing.

Typical GNSS receivers adopt scalar tracking approach where the signals of different channels are tracked independently. Scalar tracking is simple but its performance is suboptimal [33]. Vector tracking is proposed to improve the tracking performance in harsh environments [34]. It adopts a unified navigation to estimate the position, velocity and time and to generate the signal replicas of each channel. A RTK-based vector tracking PLL (RTK-VPLL) is proposed in [35], which realizes the true vector tracking of carrier phase, showing significant reliability improvement in moderate-foliage environments. Nevertheless, standalone GNSS tracking approaches always face the trade-off between the dynamic stress endurance and thermal noise suppression. The equivalent loop bandwidth should be as narrow as possible to suppress the thermal noise, but it cannot be too narrow to track the motions of the receiver.

As a result, ultra-tight integration is designed to overcome the difficulty by aiding the line-of-sight (LOS) dynamics into the tracking channels [36]. IMU is the most widely used sensor in ultra-tight integration. Theoretical models regarding the influence of varying grades of IMUs on the PLLs have been established and validated with real data [37]. Ultra-tight integration enables the tracking loops to realize long coherent integration (LCI) period and narrow loop bandwidth in dynamic scenarios, leading to superior performance in weak signal tracking [38], multipath mitigation, short-term signal blocking resistance, etc. The Ultra-tight GNSS/INS integration solution in [39] realizes sub-meter level positioning accuracy in dense forestry areas where traditional receiver technology fails to track GNSS signals. Even indoor GNSS signal tracking is possible when a high grade IMU and extreme long coherent integration periods are adopted [40]. In order to realize effective long coherent integration, another obstacle which needs to be overcome is the navigation bit transition. Mature solutions have been developed to address the problem.

The work in [41] proposes a maximum-likelihood (ML) bit estimation method to predict navigation bits in the context of GNSS/INS ultra-tightly coupled integration. In addition, Assisted-GNSS (A-GNSS) techniques can be employed to provide a stable navigation bit assistance stream [42]. For GNSS signals with dedicated pilot components, such as GPS L5 and BDS B2a/B2b, long coherent integration can be directly applied, as pilot channels are not modulated by navigation bits [43].

However, similar with LC and TC GNSS/INS integration, the rapid error accumulation of INS aggravates the system performance significantly. GNSS/INS/Vision or LiDAR ultra-tightly integration hence starts to elicit interest. Some initial research attempts to explore the GNSS/INS/Vision or LiDAR ultra-tightly integration architecture [44], [45], [46], showing its superiority to a certain extent. The work in [44] proposes an ultra-tightly coupled GNSS/INS/Vision architecture, which adopts a fuzzy control strategy to switch between a Vision-assisted GNSS/IMU ultra-tightly integrated Kalman Filter and a combined navigation filter of Vision and INS. Another ultra-tight integrated Vision aided-INS/GNSS system [45] uses a federated fusion block to fuse the GNSS/INS estimator and INS/Vision estimator. Both studies concentrate on low-accuracy code and carrier frequency (Doppler) tracking within a GNSS/INS/Vision ultra-tight integration framework, without targeting high-precision carrier phase tracking. Besides, these studies intend to exclude GNSS when the loop tracking quality is poor, rather than enhancing it through GNSS/INS/Vision ultra-tightly coupled integration. As a result, the potential of multi-sensor ultra-tight integration is not fully exploited. Moreover, existing multi-sensor ultra-tight integration studies only demonstrate preliminary results without thorough performance analysis. Merging the data processing of INS/Vision or LiDAR with the signal processing involved in GNSS signal tracking requires a deep understanding of both domains. There are few exemplary studies despite its immense potential to enhance GNSS signal tracking and high-precision positioning for intelligent transportation applications.

This work proposes a multi-sensor (GNSS/INS/Vision) ultra-tightly coupled integration system with GNSS carrier phase long coherent integration tracking (MUT-LCI) to improve the GNSS precision positioning (RTK positioning) availability radically. The GNSS/INS/Vision ultra-tightly coupled integration is adopted to eliminate the dynamic stresses endured by the receiver tracking loops. Therefore, the coherent integration period in the PLL can be extended, leading to excellent carrier phase tracking performance in challenging environments. In order to expand the pull-in range of the carrier phase discriminator, a four-quadrant discriminator is used. The data fusion of the sensors is conducted using a Multi-state Constraint Kalman Filter [47].

In contract to conventional LC or TC multi-sensor integration solutions, MUT-LCI uses the GNSS receiver as a "white box". It has the capability to enhance the signal processing of the GNSS receiver, which is the deepest form of integration navigation. It can provide robust high-precision positioning solution for the navigation of autonomous vehicles and intelligent robots in harsh, unknown and large-scale environments. Validation was conducted in an extremely challenging environment characterized by a mixture of complex Line-of-Sight (LOS), Non-Line-of-Sight (NLOS), signal blockages, and multipath effects in the GNSS signals. The original contributions of this paper are listed as follows:

1) A multi-sensor (GNSS/INS/Vision) ultra-tightly coupled integration system is proposed, which not only fuses GNSS RTK, MEMS IMU, and monocular camera data using a Multi-State Constraint Kalman Filter (MSCKF), but also leverages the estimated dynamics to assist GNSS carrier phase signal tracking. This enables the ultra-tightly coupled integration of multiple heterogeneous sensors at the GNSS baseband signal processing level.
2) Building upon the ultra-tightly coupled integration framework, this study proposes a Long Coherent Integration (LCI) GNSS Phase-Locked Loop (PLL) utilizing a four-quadrant phase discriminator. This design significantly enhances the quality of carrier phase observations by improving sensitivity and resistance to multipath effects. Moreover, the proposed LCI tracking method demonstrates a strong capability to maintain continuous signal tracking even under frequent short-term signal blockages — so long as their duration remains shorter than the coherent integration interval.
3) The performance of the proposed system (MUT-LCI) is comprehensively evaluated in challenging environments, including dense tree canopies and tall buildings. Test results indicate that a semi-tightly coupled GNSS/INS/Vision system achieves only meter level positioning accuracy under such conditions, whereas the proposed MUT-LCI system supports a coherent integration time of 300 ms, enabling robust GNSS carrier phase measurement and achieving centimeter level positioning accuracy.

II. Methodology

In this section, we elaborate on the proposed multi-sensor (GNSS/INS/Vision) ultra-tightly coupled integration system with GNSS carrier phase long coherent integration tracking. First, an overview of the system is presented. Subsequently, the technical details are introduced, including top-level GNSS RTK/INS/Vision data fusion, bottom-level ultra-tight integration implementation, Long coherent integration carrier phase tracking, VIO-assisted LCI loop model and carrier phase error discrimination with cycle slip mitigation.

A. System Overview

The GNSS/INS/Vision MUT-LCI architecture is composed of GNSS baseband processing channels, a RTK positioning algorithm, a visual-inertial odometry, a top-level Kalman filter and an ultra-tight integration module. The overall diagram is shown in Fig. 1. Baseband channels process the GNSS signals. Each of them tracks the signal of a specific satellite, generating corresponding pseudo-range, Doppler and carrier phase observations.

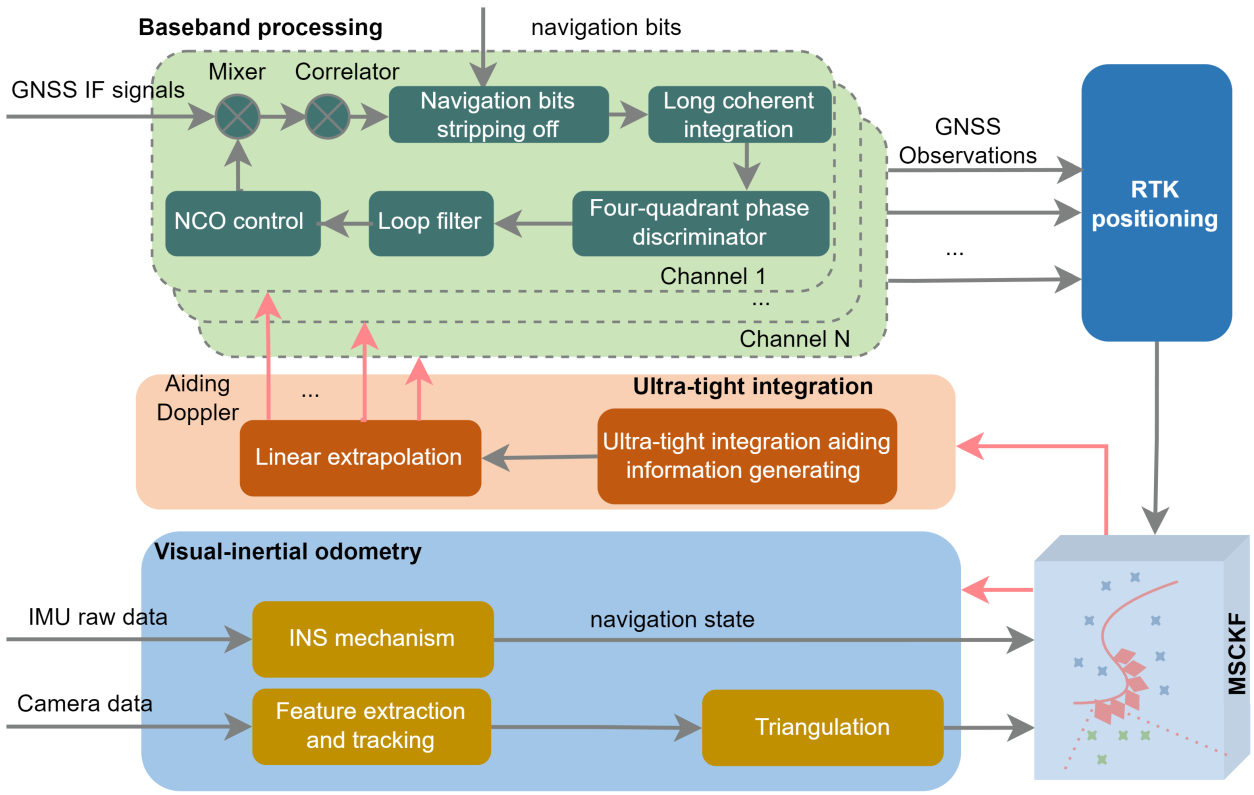

Fig. 1. Structure of multi-sensor (GNSS/INS/Vision) ultra-tightly coupled system with GNSS carrier phase long coherent integration tracking (MUT-LCI).

All the channels' observations are sent to a RTK positioning algorithm where the receiver's position, velocity and time are estimated. The information fusion is conducted at two levels. One is the top data processing level where a Multi-state Constraint Kalman Filter (MSCKF) is used to fuse the IMU state propagation result, visual feature measurements and GNSS RTK measurements, as shown in the MSCKF block in Fig. 1. The other is the bottom signal processing level where the Doppler caused by the satellite-receiver relative motion is estimated and used to control the numerically controlled oscillator (NCO) of the tracking loop, compensating for external dynamic stresses, as shown in the ultra-tight integration block in Fig. 1.

The structure is a semi-tightly coupled Kalman Filter-based GNSS/INS/Vision ultra-tight integration, which is straightforward and has light processing load [48]. The top-level GNSS/INS/Vision data integration is conducted in a semi-tight way. A tightly coupled INS/Vision integration scheme is employed to construct a Visual-Inertial Odometry (VIO) module, whereas the RTK position measurements are integrated through a loosely coupled approach. At the bottom level of GNSS signal processing, the motions of the receiver and satellites are estimated by the top-level integration module and injected into the local PLLs, realizing multi-sensor ultra-tightly coupled integration. The INS is selected to serve as the bridge between the top- and bottom-level fusion modules, owing to its ability to provide continuous, high-frequency measurements across various environments. On one hand, the IMU acts as the core sensor to propagate the navigation state and other sensors provide the measurements to update the MSCKF. MSCKF is essentially an optimized Extended Kalman Filter (EKF) for real-time vision-aided navigation [47]. The visual system supplies measurements to the MSCKF, forming a Visual-Inertial Odometry (VIO) system in conjunction with the INS. After feature tracking and triangulation, the visual feature measurement model is established. Then a left nullspace projection is carried out to establish the constraints of multiple camera poses. Finally, the MSCKF updates are conducted to generate the integrated navigation output and calibrate the INS errors. Meanwhile, whenever a GNSS RTK positioning result is received, the corresponding measurement model will also be established and used to update the EKF. On the other hand, the ultra-tight integration relies on the high frequency IMU navigation states to estimate the aiding information for tracking loops. The aiding information ought to be extrapolated first due to the rapidly varying dynamics. Then it will be injected into the tracking loop to eliminate the dynamic stress. Ultra-tightly coupled integration makes the tracking loop work under quasi-static conditions, facilitating longer coherent integration periods. Long coherent integration carrier phase tracking refers to the technique that a PLL performs a coherent integration period longer than a certain interval (usually 20 ms, the length of a navigation bit). Increasing coherent integration time is the radical way to enhance the signal to noise ratio (SNR), providing superior performance in weak signal tracking, frequent short-term (less than one coherent integration period) blockage resistance, multipath mitigation, etc. In order to overcome the navigation

bit transition problem during long coherent integration, an external navigation bit resource is adopted. Besides, we use a four-quadrant carrier phase discriminator, instead of a traditional Costas discriminator, to estimate the carrier phase error. The four-quadrant carrier phase discriminator has the widest tracking range $(-\pi, \pi)$ and can eliminate half-cycle slips compared to Costas discriminators $(-\pi/2, \pi/2)$.

B. Top-Level GNSS RTK/INS/Vision Data Fusion

The top level fusion of RTK, INS and vision is conducted with a multi-state constraint Kalman filter. It is an optimized EKF which establishes the geometric constraints of multiple camera poses that observe a common visual feature. The tracking features can hence be removed from the system state vector, resulting in significant processing efficiency improvement. The MSCKF is the optimal top level integration technique for an ultra-tight integration architecture because of its capability to process data in time and to provide tracking loop aiding information with low time delay.

The IMU state of the k_{th} epoch is described as:

$$\mathbf{x}_{IMU,k} = \left[\mathbf{q}_k^T \ \mathbf{p}_{b_k}^T \ \mathbf{v}_{b_k}^T \ \mathbf{b}_{g,k}^T \ \mathbf{b}_{a,k}^T \right]^T \tag{1}$$

where $\mathbf{q}_k$ is the IMU attitude, $\mathbf{p}_{b_k}$ and $\mathbf{v}_{b_k}$ denote the position and velocity, $\mathbf{b}_{g,k}$ and $\mathbf{b}_{a,k}$ are the gyroscope and accelerometer bias, respectively. The corresponding error-state is expressed as:

$$\widetilde{\mathbf{x}}_{IMU,k} = \left[\widetilde{\boldsymbol{\theta}}_k^T \ \widetilde{\mathbf{p}}_{b_k}^T \ \widetilde{\mathbf{v}}_{b_k}^T \ \widetilde{\mathbf{b}}_{g,k}^T \ \widetilde{\mathbf{b}}_{a,k}^T \right]^T \tag{2}$$

The error model of the IMU state is expressed as:

$$\dot{\widetilde{\mathbf{x}}}_{IMU} = \mathbf{F}\widetilde{\mathbf{x}}_{IMU} + \mathbf{G}\mathbf{n}_{IMU} \tag{3}$$

where $\mathbf{n}_{IMU}$ is the system noise, $\mathbf{F}$ and $\mathbf{G}$ are constant matrices.

The MSCKF maintains a window where a specific number of camera poses are augmented to the IMU state vector, which is shown in Eq. (4):

$$\mathbf{x}_k = \left[\mathbf{x}_{IMU,k}^T \ \mathbf{q}_{c_1}^T \ \mathbf{p}_{c_1}^T \cdots \mathbf{q}_{c_n}^T \ \mathbf{p}_{c_n}^T \right]^T \tag{4}$$

where $\left[\mathbf{q}_{c_i}^T \mathbf{p}_{c_i}^T\right]$ is the i_{th} augmented attitude and position of the camera. The system covariance is expressed as:

$$\mathbf{P}_k = \begin{bmatrix} \mathbf{P}_{I_k} & \mathbf{P}_{I_k C_k} \\ \mathbf{P}_{C_k I_k} & \mathbf{P}_{C_k} \end{bmatrix} \tag{5}$$

where $\mathbf{P}_{I_k}$ and $\mathbf{P}_{C_k}$ denotes the variance of the IMU and augmented states, respectively, and $\mathbf{P}_{I_k C_k}$ is the covariance matrix of the IMU and augmented states.

When a visual feature fails to maintain tracking or its continuous tracking time exceed the length of the sliding window, it will be utilized to update the EKF. The augmented states will be used for the triangulation of the features. The position of the j_{th} feature point in the i_{th} image is denoted as:

$$\mathbf{p}_{f_j}^p = \mathbf{h}_d \left(\mathbf{h}_p \left(\mathbf{h}_t \left(\mathbf{R}_{b_i}, \mathbf{p}_{b_i}, \mathbf{p}_{f_j}, \mathbf{R}_b^c, \mathbf{p}_c^b \right), \mathbf{K} \right), \boldsymbol{\zeta} \right) \tag{6}$$

where the superscript p of $\mathbf{p}_{f_j}^p$ denotes that the feature point is projected in to the image coordinate. $\mathbf{h}_t(\cdot)$ transforms the features' positions in the navigation frame $(\mathbf{p}_{f_j})$ into the camera frame $(\mathbf{p}_{f_j}^{c_i})$. $\mathbf{R}_{b_i}$ and $\mathbf{p}_{b_i}$ are the attitude and position of the IMU, which will be combined with the camera-IMU extrinsics $\mathbf{R}_b^c, \mathbf{p}_c^b$, to calculate the camera pose and position. $\mathbf{h}_p(\cdot)$ and $\mathbf{h}_d(\cdot)$ denote the projection and distortion function of the imaging process. $\mathbf{K}$ and $\boldsymbol{\zeta}$ are the camera intrinsics and distortion parameters, respectively.

Given the nested projection model, the Jacobian of the feature measurement respect to the state can be derived:

$$\frac{\partial \mathbf{p}_{f_j}^p}{\partial \mathbf{x}} = \frac{\partial \mathbf{h}_d}{\partial \mathbf{z}_{f_j}} \frac{\partial \mathbf{h}_p}{\partial \mathbf{p}_{f_j}^{c_i}} \frac{\partial \mathbf{h}_t}{\partial \mathbf{x}} \tag{7}$$

Then a perturbation analysis with respect to the IMU state and feature position is conducted, resulting in the measurement model of the visual feature:

$$\mathbf{z}_p = \mathbf{H}_x \widetilde{\mathbf{x}} + \mathbf{H}_f \widetilde{\mathbf{p}}_{f_j} + \mathbf{n}_p \tag{8}$$

A nullspace projection is carried out to remove the matrix $\mathbf{H}_f$ from the measurement model, decreasing the processing load significantly, which is shown in Eq. (9):

$$\mathbf{z}_p^o = \mathbf{H}_x^o \widetilde{\mathbf{x}} + \mathbf{n}_p^o \tag{9}$$

Afterwards, the standard EKF update can be done, and a QR decomposition is typically adopted to further increase the computing efficiency.

Every time a RTK result arrives, the GNSS position update is conducted. The predicted antenna position $\mathbf{p}_{RTK}^n$ with respect to the IMU position is described as:

$$\mathbf{p}_{RTK}^n = \mathbf{p}_b^n + \mathbf{R}_b^n \mathbf{l}_{ant}^b \tag{10}$$

where the $\mathbf{l}_{ant}^b$ is the lever arm between the GNSS antenna and the IMU. Similarly, a perturbation analysis is conducted to derive the GNSS position measurement model:

$$\mathbf{z}_{RTK} = -\widetilde{\mathbf{p}}_b^n + \mathbf{R}_b^n \left[\mathbf{l}_{ant}^b\right]_\times \widetilde{\boldsymbol{\theta}} + \mathbf{n}_{RTK} \tag{11}$$

As the carrier phase observations offer significantly greater accuracy than Doppler observations, only fixed RTK positioning results are incorporated into the EKF.

C. Bottom-Level Ultra-Tight Integration Implementation

An ultra-tightly coupled GNSS/INS/Vision integration algorithm is established as the foundational component to enable longer coherent integration durations. In this work, we propose to use INS as the central axis to furnish ultra-tight loop aiding information. Every time a new image or RTK positioning result is received, the errors of the IMU will be calibrated, maintaining continuous high precision positioning output. The INS mechanism derives the velocity and position of the IMU from the measured angular rate and specific force. The discrete-time velocity update can be expressed as:

$$\mathbf{v}_k^{\mathrm{n}} = \mathbf{v}_{k-1}^{\mathrm{n}} + \Delta \mathbf{v}_{\mathbf{f},k}^{\mathrm{n}} + \Delta \mathbf{v}_{\mathrm{g/cor},k}^n \tag{12}$$

where $\mathbf{v}_k^{\mathrm{n}}$ and $\mathbf{v}_{k-1}^{\mathrm{n}}$ denote the k_{th} and $k-1_{th}$ IMU velocity in navigation frame. $\Delta \mathbf{v}_{\mathbf{f},k}^{\mathrm{n}}$ is the velocity increment due to the gravity and Coriolis force. $\Delta \mathbf{v}_{\mathrm{g/cor},k}^n$ represents the velocity increment due to the specific force. In the meantime, the average acceleration of the IMU in n-frame is estimated:

$$\mathbf{a}_k^{\mathrm{n}} = \left(\Delta \mathbf{v}_{\mathbf{f},k}^{\mathrm{n}} + \Delta \mathbf{v}_{\mathrm{g/cor},k}^n \right) / dt \tag{13}$$

where dt is the sampling period of the IMU. The position is expressed as the quaternion from the navigation frame to the Earth Centered, Earth Fixed (ECEF) frame [49], and the update algorithm is shown in Eq. (14):

$$\mathbf{q}_{\mathrm{n}(k)}^{\mathrm{e}(k)} = \mathbf{q}_{\mathrm{e}(k-1)}^{\mathrm{e}(k)} \otimes \mathbf{q}_{\mathrm{n}(k-1)}^{\mathrm{e}(k-1)} \otimes \mathbf{q}_{\mathrm{n}(k)}^{\mathrm{n}(k-1)} \tag{14}$$

where $\mathbf{q}_{\mathrm{n}(k)}^{\mathrm{e}(k)}$ is the position quaternion of the k_{th} epoch. $\mathbf{q}_{\mathrm{e}(k-1)}^{\mathrm{e}(k)}$ and $\mathbf{q}_{\mathrm{n}(k)}^{\mathrm{n}(k-1)}$ denote the rotation of ECEF-frame and n-frame respectively. The quaternion multiplication is indicated as $\otimes$. As the velocity has been updated, the height can be updated by Eq. (15):

$$h_k = h_{k-1} - v_{\mathrm{D},k-1/2}\Delta t_k \tag{15}$$

where the midway velocity $\mathbf{v}_{k-1/2}^{\mathrm{n}} = \frac{1}{2}\left(\mathbf{v}_{k-1}^{\mathrm{n}} + \mathbf{v}_{k}^{\mathrm{n}}\right)$ is updated by interpolation. After lever arm compensation, the receiver position, velocity and acceleration can be derived, denoted as $\mathbf{P}_{\mathrm{U}}^{e}$, $\mathbf{V}_{\mathrm{U}}^{e}$, and $\mathbf{a}_{\mathrm{U}}^{e}$.

The ultra-tight integration aiding Doppler is composed of two components, shown in Eq. (16):

$$f_{UT} = f_S^{(i)} - f_U \tag{16}$$

where $f_S^{(i)}$ and f_U denote the Doppler induced by motions of the i_{th} satellite and receiver, respectively. Receiver motion induced Doppler is expressed as:

$$f_U^{(i)} = \frac{\mathbf{I}_{S,U} \cdot \mathbf{V}_U^e}{\lambda_c} \tag{17}$$

where λ_c is the wavelength of the GNSS signals. $\mathbf{I}_{S,U}$ is the unit vector in the LOS direction between the receiver and i_{th} satellite in ECEF-frame, which can be denoted as:

$$\mathbf{I}_{S,U} = \frac{\mathbf{P}_S^{(i),e} - \mathbf{P}_U^e}{\left\|\mathbf{P}_S^{(i),e} - \mathbf{P}_U^e\right\|} \tag{18}$$

where $\mathbf{P}_S^{(i),e}$ is the position of the i_{th} satellite which is provided by the RTK positioning algorithm.

Although the sampling frequency of an IMU varies from dozens to hundreds of hertz, it is still not enough to compensate for the rapid dynamic fluctuations endured by the tracking loops, especially for the high dynamic robotic applications, such as quadrotors. Therefore, a linear extrapolation of the receiver motion induced Doppler is conducted. Assume the sampling period of the IMU is denoted as T_{INS}, and the acceleration remains constant during an IMU sampling interval. Then the extrapolation is expressed as:

$$f_U\left(kT_{INS} + t\right) = f_U\left(kT_{INS}\right) - \frac{\mathbf{I}_{S,U} \cdot a_{\mathrm{U}}^e}{\lambda_c} \cdot t \tag{19}$$

Similarly, the Doppler due to the satellite motion is denoted as:

$$f_S^{(i)} = \frac{\mathbf{I}_{S,U} \cdot \mathbf{V}_S^{(i),e}}{\lambda_c} \tag{20}$$

where $\mathbf{V}_S^e$ denotes the satellite's velocity. An extrapolation is also conducted:

$$f_S^{(i)}\left(kT_P + t\right) = f_S^{(i)}\left(kT_P\right) + \frac{f_S^{(i)}(k) - f_S^{(i)}(k-1)}{T_P} \cdot t \tag{21}$$

where T_P is the positioning period. The update rate of the ultra-tight integration aiding Doppler (f_{UT}) should be large enough to compensate for the loop dynamics effectively. In our experiment, the ultra-tight aiding Doppler update rate was set as 1000 Hz, which is equal to the update rate of the code correlator to maximize the aiding performance. Still, the ultra-tight aiding Doppler update rate can be adjusted based on the specific dynamics of the robot and the computing power of the processor. Whenever the aiding Doppler is updated, it will be used to control the NCO of the local loop. As a result, the local loop should only track the residuals of the dynamics, which makes longer coherent integration periods and narrower bandwidths possible.

D. Long Coherent Integration Carrier Phase Tracking

The coherent integration is also referred to as the predetection integration. This refers to the signal processing stage after the Intermediate Frequency (IF) signal has been processed by the carrier mixer and code correlator, but before the phase discriminator. The GNSS IF signal is a complex signal with the inphase (I) and quadrature (Q) component, which is denoted as:

$$\begin{aligned} s_{IF,I}^{(i)} &= c(t)D(t)\cos\left(2\pi\left(f_{IF} + f_d\right)t + \theta_I\right) + n_{IF,I} \\ s_{IF,Q}^{(i)} &= c(t)D(t)\sin\left(2\pi\left(f_{IF} + f_d\right)t + \theta_Q\right) + n_{IF,Q} \end{aligned} \tag{22}$$

where the $c(t)$ is the pseudo-random code, and $D(t)$ is the navigation bit. f_{IF} and f_d denote the intermediate frequency and signal Doppler. $\theta_{I/Q}$ is the initial phase of the IF signal. $n_{IF,I}$ and $n_{IF,Q}$ are the addictive white Gaussian noises. After carrier and code stripping processes, the signal will be integrated to suppress noise, gaining improved SNR. Assume the coherent integration starts at t_0, then the continuous-time coherent integration signal is expressed as:

$$\begin{aligned} \Phi_I(n) &= D(n)sinc\left(f_e T_{coh}\right)\cos\left(\phi_e\right) + n_{coh,I} \\ \Phi_Q(n) &= D(n)sinc\left(f_e T_{coh}\right)\sin\left(\phi_e\right) + n_{coh,Q} \end{aligned} \tag{23}$$

where the T_{coh} is the coherent integration period, f_e and $\phi_e = 2\pi f_e\left(t_0 + \frac{T_{coh}}{2}\right) + \theta_e$ denote the average frequency and phase error during the integration period, respectively. The addictive white Gaussian noise items are expressed as $n_{coh,I}$ and $n_{coh,Q}$. The coherent integration interval cannot exceed the length of a navigation bit (for example, 20 ms for GPS L1 signals) without a prior knowledge of the bit polarity. Mature solutions of this issue have been proposed and validated, including bit prediction methods, Assisted GNSS (AGNSS), etc. Besides, new GNSS signals, such as BDS B2a/b, Galileo E5a/b, are modulated with dataless pilot components, which can realize long coherent integration without external assistance. In this work, we used an external navigation bit flow $\widetilde{D}(n)$ to eliminate the influence of bit transitions.

After bit synchronization, a short-term coherent integration with a duration equal to that of a navigation bit is performed in the first place. The corresponding discrete-time signal after short-term coherent integration is expressed as:

$$\begin{aligned} I(n) &= sinc\left(f_{e,n}T_{Bit}\right)\cos\left(\phi_{e,n}\right) + n_{Bit,I} \\ Q(n) &= sinc\left(f_{e,n}T_{Bit}\right)\sin\left(\phi_{e,n}\right) + n_{Bit,Q} \end{aligned} \tag{24}$$

where T_{Bit} is the length of a navigation bit. $n_{Bit,I}$ and $n_{Bit,Q}$ are the noise items. Then the coherent integration of N_L successive

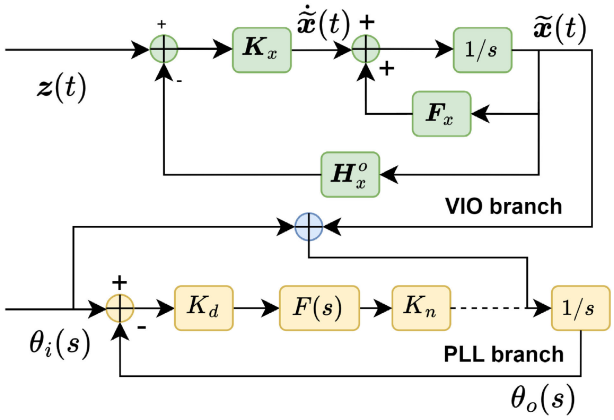

Fig. 2. VIO-assisted LCI PLL model in Laplace domain.

bits will be carried out, generating the long coherent integration signal with an integration period of T_{LCI} ($= N_L \cdot T_{Bit}$), which is denoted as:

$$I_{LCI}(k) = \sum_{n=1}^{N_L} \widetilde{D}\left[(k-1)N_L + n\right] I\left[(k-1)N_L + n\right]$$
$$Q_{LCI}(k) = \sum_{n=1}^{N_L} \widetilde{D}\left[(k-1)N_L + n\right] Q\left[(k-1)N_L + n\right] \quad (25)$$

The noise of the coherent integration signal is modelled as white Gaussian noise of zero mean and variance of σ^2. On one hand, when N_L times of integration periods are conducted, the signal magnitude is scaled by N_L times, indicating an ${N_L}^2$-fold increase in signal power. On the other hand, the power of the white Gaussian noise only increases by N_L times during the process. As a result, the long coherent integration improves the signal SNR by N_L times, which enables accurate and continuous tracking of extreme weak signals. Besides, as shown in Eq. (23), the magnitude of the predetection signal is a *sinc* function of the frequency error. The signal energy drops to zero when the frequency error reaches $1/T_{coh}$, which indicates that longer coherent integration periods result in a thinner and steeper main peak of the sinc-squared characteristic. Hence, the long coherent integration makes the LOS signal peak more distinguishable from other signal peaks due to the multipath effects, resulting in superior multipath mitigation performance.

E. VIO-Assisted LCI Loop Model

As previously described, the VIO provides ultra-tight aiding information with enhanced robustness and accuracy, particularly in challenging environments. Compared to standalone INS assistance, the VIO assistance enables more effective suppression of dynamic stress within the PLL, thereby supporting longer coherent integration durations. In this subsection, a simplified mathematical model of the VIO-assisted LCI PLL is established to analyze its tracking performance. The model of the VIO-assisted LCI PLL in Laplace domain is shown in Fig. 2. The upper part illustrates the VIO branch, and the lower part is the LCI PLL branch. $\mathbf{K}_x$ denotes the Kalman gain matrix. K_d and K_n are the loop filter gain and NCO gain, respectively. The NCO of the LCI PLL is modeled as $1/s$, which accepts control information from two resources: the ultra-tight integration aiding information from the VIO branch and the loop filter output from the local PLL branch. The two resources control the NCO asynchronously. In the accumulation stage of long coherent integration, only the VIO branch provides the NCO control information. Hence, the line from the K_n to $1/s$ is dashed. Every time the LCI PLL completes a closed-loop update, the dynamic residuals caused by the aiding information errors are estimated by the loop discriminator and used to control the NCO after filtering, which can be regarded as a "reset" process [37]. Hence, this subsection primarily analyzes the error divergence characteristics of the aiding information during the accumulation stage of the long coherent integration.

In Laplace domain, the VIO branch is modelled as a Continuous-Time Kalman Filter, and the evolution of the error covariance matrix is described by a Riccati differential equation:

$$\dot{\mathbf{P}}(t) = \lim_{T_{VIO}\to 0} \frac{\mathbf{P}_k - \mathbf{P}_{k-1}}{T_{VIO}} \quad (26)$$

where T_{VIO} is the update period of the Visual-Inertial Odometry. However, even for general linear time-varying systems, solving the Riccati equation in Eq. (26) is highly challenging and may not yield a closed-form solution. Moreover, the VIO system exhibits strong nonlinearity, further increasing the complexity of solving the associated equations and preventing a direct analytical expression of tracking errors under VIO assistance. Therefore, an experimental analysis of the MSCKF covariance matrix was conducted to analyze the error divergence characteristics of the VIO branch. A set of experimental data (including GNSS positioning, MEMS IMU and monocular camera data) was collected along a trajectory oriented in the north–south direction, then the data was processed by the Top-level RTK/INS/Vision integration algorithm introduced in Section II-B. Both GNSS/INS/Vision (GNSS/VIO) and GNSS/INS integration modes are tested. The error covariance matrices from the GNSS/INS/Vision and GNSS/INS integration modes are analyzed, investigating the VIO's contribution to enhance the ultra-tight integration performance. It is noted that this test is only conducted on the top data processing level, and the covariance matrix directly reflects the accuracy of the ultra-tight integration aiding information from the VIO branch.

Ban et al. [37] has made a quantitative analysis of GNSS/INS ultra-tight integration tracking loops, which indicates that the initial velocity and attitude errors are major factors that affect the tracking accuracy. Equation (17) also indicates that the velocity of the vehicle effects the performance of ultra-tight integration directly. As the experimental trajectory is in the north-south direction, the north velocity and yaw angle of the vehicle have the greatest influence on the accuracy of the ultra-tight aiding Doppler, so their variances are analyzed in detail.

Figure 3 shows the variances of the north velocity and yaw angle. It is obvious that the variance of the GNSS/INS/Vision integration is smaller than that of the GNSS/INS integration,

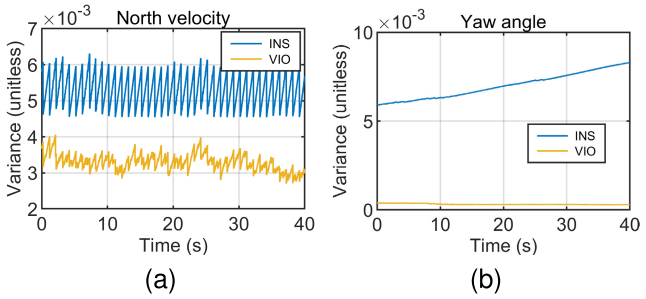

Fig. 3. Variances of the north velocity and yaw angle. Legend "VIO" and "INS" denote the GNSS/INS/Vision and GNSS/INS integration mode, respectively. (a) Variance of the north velocity (b) Variance of the yaw angle.

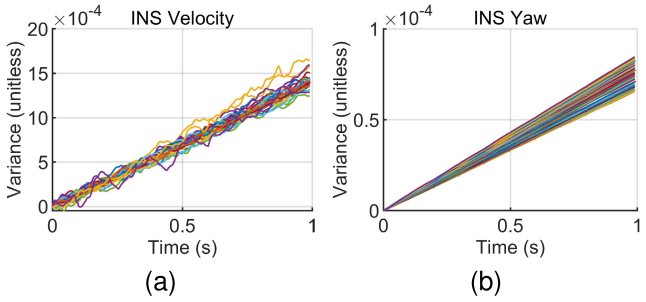

Fig. 4. The variances of INS within one second. (a) Variance of the north velocity (b) Variance of the yaw angle.

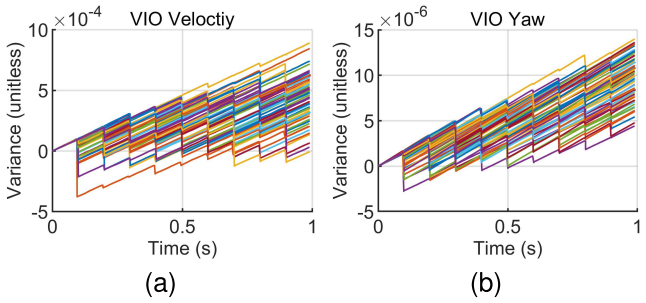

Fig. 5. The variances of VIO within one second. (a) Variance of the north velocity (b) Variance of the yaw angle.

which proves that the multi-sensor integration can improve the positioning accuracy, thus generating ultra-tight aiding information with improved accuracy. Another phenomenon worth noting is that every time the GNSS measurement arrives, it will be used to update the EKF, providing absolute corrections at a frequency of, in this case, 1Hz. The error state estimation is considered to be reset at each GNSS update epoch. As a result, the variance curves exhibit sawtooth patterns. Between two successive epochs, the divergence of the variance shows the performance of the two dead reckoning systems: INS and VIO.

In order to further investigate the divergence characteristics of the INS and VIO within two successive GNSS update epochs, based on the results shown in Fig. 3, sixty 1-second samples were extracted. The variance after each GNSS correction was set to zero, and all samples were plotted together, as illustrated in Fig. 4 and Fig. 5.

Figure 4 shows the divergence characteristics of the error variance for the INS over 1-second intervals. In the absence of external correction information, pure INS exhibits rapid divergence in both velocity and heading estimates, which is why the GNSS/INS ultra-tight integration cannot fulfill the precision requirements for long coherent integration carrier phase tracking. On the contrary, as shown in Fig. 5, every time a key frame arrives, the visual measurements will be used to update the MSCKF, correcting the INS errors. Visual measurements, which capture both translational and rotational motion, offer significant corrections to velocity and heading errors. The strength of these corrections depends on environmental textures, as well as the quantity and quality of tracked feature points. As a result, the corrections exhibit a certain degree of randomness. It is worth noting that the MSCKF employs a delayed update mechanism, which may lead to abrupt changes in the state variables, as the curves in Fig. 5 shows. The abrupt changes may introduce a disturbance to the tracking loop, leading to a degradation in tracking stability. Since the magnitude of the state correction is known, it can be compensated for before the ultra-tight integration aiding information is delivered to the phase-locked loop NCO. In the proposed MUT-LCI system, the modification of the state variables is obtained from the MSCKF output, and a corresponding frequency step is applied to the aiding information to compensate for the abrupt changes, thereby eliminating their impact on the carrier tracking loop [50]. To sum up, compared with pure INS assistance, the VIO-based ultra-tight integration is able to provide PLL aiding information with better accuracy and robustness, thus significantly improving the long coherent integration carrier phase tracking performance.

F. Carrier Phase Error Discrimination With Cycle Slip Mitigation

The predetection signal is sent to a discriminator to estimate the carrier phase error. Typical arctangent discriminator (Atan) used in Costas PLLs is denoted as:

$$\varphi_{\text{atan}} = \arctan\left(\frac{Q_{Loco}}{I_{Loco}}\right) \tag{27}$$

The Atan discriminator returns carrier phase error measurements in the interval $(-\pi/2, +\pi/2)$, and it is insensitive to the presence of data modulation. However, the pullin range ($-\pi/2$ to $\pi/2$) of the Atan discriminator is too narrow for harsh environments. When an input phase error larger than $\pi/2$ is received, the Atan discriminator cannot produce an accurate estimate, which is likely to cause a cycle slip.

In this paper, a four-quadrant carrier phase discriminator (Atan2) is adopted, which is expressed as:

$$\varphi_{atan2} = \text{atan2}\,(Q_{Loco}, I_{Loco}) \tag{28}$$

Atan2 is the optimal phase discriminator when navigation data bit wipe-off is conducted. It has a pull-in range from $-\pi$ to π, permitting accurate tracking of the full four quadrant range of the pre-detection signal. Therefore, the cycle slips due to the narrow pull-in range of Atan discriminators can be avoided.

Since the Atan2 discriminator estimate full four quadrant range of the long coherent integration signal, a signal

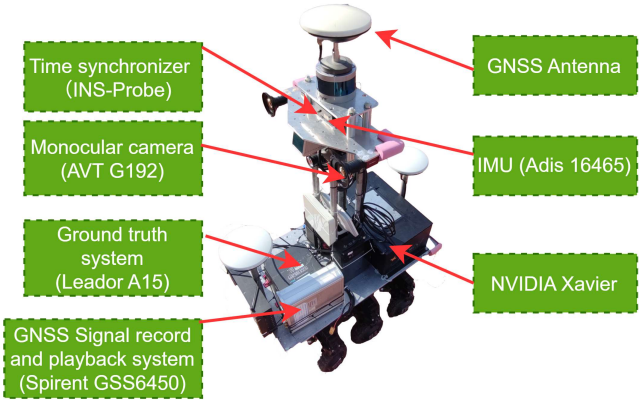

Fig. 6. Experimental intelligent transportation robot platform with key components.

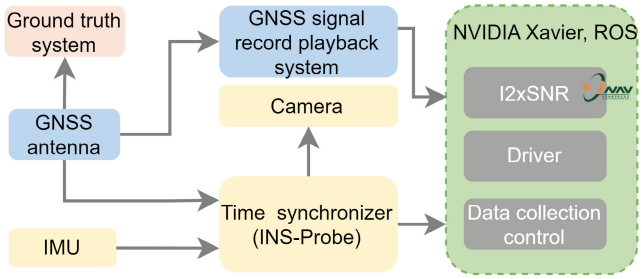

Fig. 7. The hardware connection of the MUT-LCI system.

abnormality indicator is proposed to control the extraction of the carrier phase observations, which is expressed as:

$$\varphi_{cs}(k) = \varphi_{\text{atan2}}(k) - \varphi_{\text{atan2}}(k-1) \tag{29}$$

Typically, monitoring the change rate of the carrier phase observation is used to detect the signal abnormality. In this work, the signal level indicator φ_{cs} is adopted, which is more straightforward and can rapidly response the signal alteration. When φ_{cs} exceeds a predefined threshold(π, half a cycle), the signal abnormality is determined as positive, which indicates that a cycle slip is highly likely to have happened. The carrier phase observation of this epoch will be determined as an error and not be used in the RTK positioning.

III. Experiment Setup

The experiment data were collected and processed on a wheeled robot shown in Fig. 2. This platform serves as a versatile testbed for intelligent transportation applications, including autonomous vehicles and smart delivery robots. A NVIDIA Xavier is used as the central processing unit which controls the data collection. The collected multi-sensor data would be processed with a software defined GNSS/INS/Vision ultra-tightly coupled receiver (I2xSNR) developed by our I2Nav Group.

The hardware connection is shown in Fig. 7 high precision position and orientation system (POS), Leador A15, was adopted as the ground truth system which is composed of a multi-constellation multi-frequency GNSS receiver, a navigation-grade IMU and a wheeled odometer(ODO). GNSS

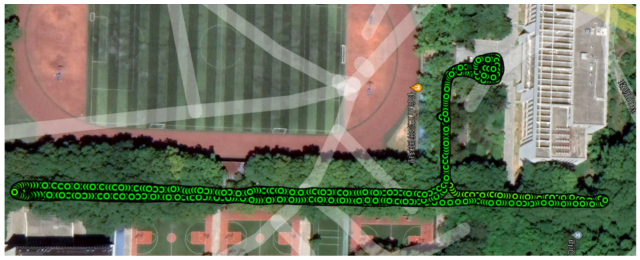

Fig. 8. The ground truth trajectory of the experiment, which is under dense tree foliage.

signals were recorded by a GNSS signal record system, Spirent GSS6450 [51], which down-converted the ratio frequency signals into intermediate frequency using the built-in oven-controlled crystal oscillator (OCXO). The GNSS signal recording bandwidth was set as 30 MHz, and the IF signal sampling rate was 30.69 MHz. The OCXO's short term stability is 100 ppm over 1 second. A monocular camera AVT G192 was used to collect gray scale images. A MEMS IMU ADIS16465 was adopted. All data was synchronized to GPS time by a self-developed hardware module called INS-probe, which integrates a GNSS receiver chip ublox-F9P [52] and the ADIS16465. Apart from that, GNSS observations from a Continuously Operating Reference Station (CORS) receiver, the Panda PD318, were recorded for RTK positioning. The baseline length is approximately 3 kilometers.

The test field was set at a highly challenging area for GNSS positioning in Wuhan University, Hubei, China. The average speed of the robot was around 1.2 m/s, and the maximum acceleration and rotation rate were about 13 m/s^2 and 1 rad/s, respectively. The trajectory is shown in Fig. 8 and the length of the test was around 20 minutes. The entire road was under dense foliage where the GNSS signals were significantly interfered. The ground truth trajectory was obtained using a post-processing RTK/INS/ODO integration software. Initially, gross errors in the multi-constellation, multi-frequency RTK positioning results were manually eliminated. Subsequently, forward RTK/INS/ODO integration was performed, and the resulting outputs were refined using a Rauch-Tung-Striebel (RTS) smoother, ensuring a high-precision and reliable ground truth trajectory. The satellite skyplot is shown in Fig. 9. Only GPS L1 and BDS B1I signals were processed, sparing the enhancement from multi-constellation multi-frequency GNSS. It is worth noting that although GPS L1 and BDS B1 signals are selected as representatives for performance evaluation, the proposed method is also applicable to other GNSS constellations and frequency bands. Several snapshots of the experiment environment are depicted in Fig. 10, including the complete covering of tree canopies and building blockage. The tree leaves would weaken the signal strength, and the tree branches and trunks would frequently block the signals. GNSS signals would be reflected by the building with abundant glass windows, causing serious multipath. The performance of the proposed MUT-LCI architecture will be evaluated thoroughly in these typical scenarios.

Figure 11 shows the carrier-to-noise-density ratio (C/N_0) measurements of three representative GPS and BDS satellites

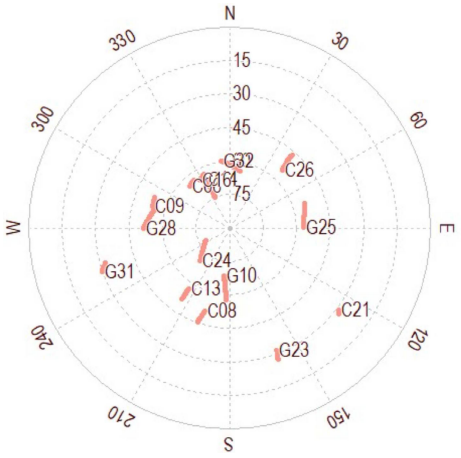

Fig. 9. Satellite skyplot of the experiment. GPS L1 and BDS B1I signals are tracked.

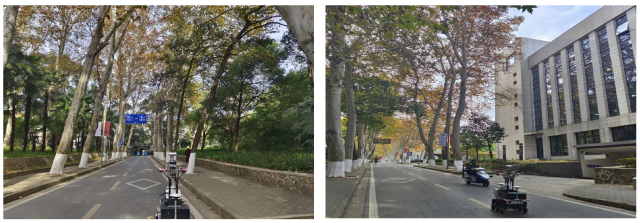

Fig. 10. Snapshots of the experiment environment, including dense tree canopies (left) and buildings (right).

during the experiment. The C/N_0 measurements remained relatively stable only during the initialization phase. Once the wheeled robot entered the dense tree-covered avenue, significant fluctuations occurred due to severe signal attenuation, frequent blockages, and multipath effects. According to [53], the disturbances in GNSS signals under dense foliage include signal strength attenuation and different patterns of multipath effects, which is the reason why the C/N_0 measurements fluctuate severely. In this scenario, maintaining reliable carrier phase tracking is particularly difficult, posing a major challenge to high-precision positioning for autonomous vehicles, such as self-driving cars and smart delivery robots.

IV. Results and Discussion

A. MUT-LCI Tracking Performance Analysis

Longer integration periods correspond to better performance of weak signal tracking and multipath resistance. Effective long coherent integration requires accurate signal dynamic compensation within the integration interval, which is conducted by the ultra-tight integration.

We carried out the experiment to evaluate the influence of different coherent integration periods in terms of signal energy accumulation and tracking performance. Figure 12 shows the PLL discriminator output of different coherent integration time, including 20 ms/ 3 Hz, 100 ms/ 1 Hz and 300 ms/ 0.6 Hz. Results from six representative satellites are presented, comprising three from the GPS and three from the BDS, and these satellites span a range of elevation angles, from relatively high (above 60°) to low (around 45°).

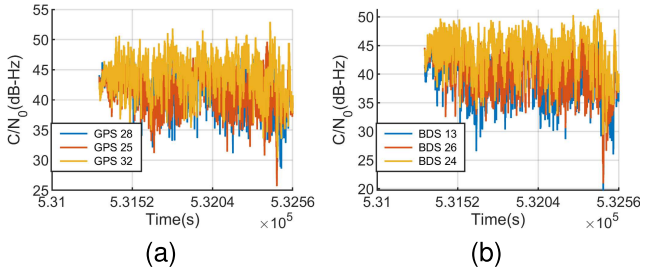

Fig. 11. The satellite carrier-to-noise-density ratio (C/N_0) measurements of the experiment. (a) GPS representative satellites (b) BDS representative satellites.

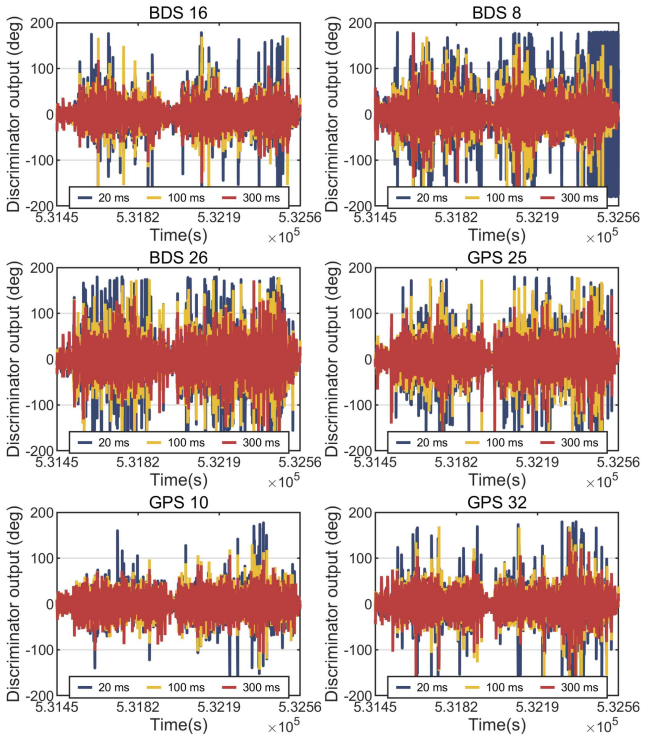

Fig. 12. Discriminator output of 6 representative satellites. Extended coherent integration periods showcase greater performance.

As the dynamic stress has been eliminated by the GNSS/INS/Vision ultra-tight integration, and a relatively stable OCXO is utilized, effective coherent integration time of 300 ms was achieved. A common pattern is clearly demonstrated in each satellite that as the coherent integration increases and the loop bandwidth decreases, the discriminated carrier phase error decreases slightly, showing better tracking performance. Moreover, the large phase jumps usually indicate tracking errors and the happening of cycle slips. The 20 ms of coherent integration period exhibits the most frequent large phase jumps, followed by 100 ms, while the tracking outcome of 300 ms demonstrates minimum occurrences of cycle slips. It is noted that the BDS 8 satellite's discriminator output of the 20 ms integration period shows a period of continuous large phase jumps, which indicates a loss of lock. On the contrary, 100 and 300 ms of integration periods can track the signal stably. Another phenomenon worthy of attention is that the discriminator output noise of different satellites is also different, which is due to the different elevation angles of

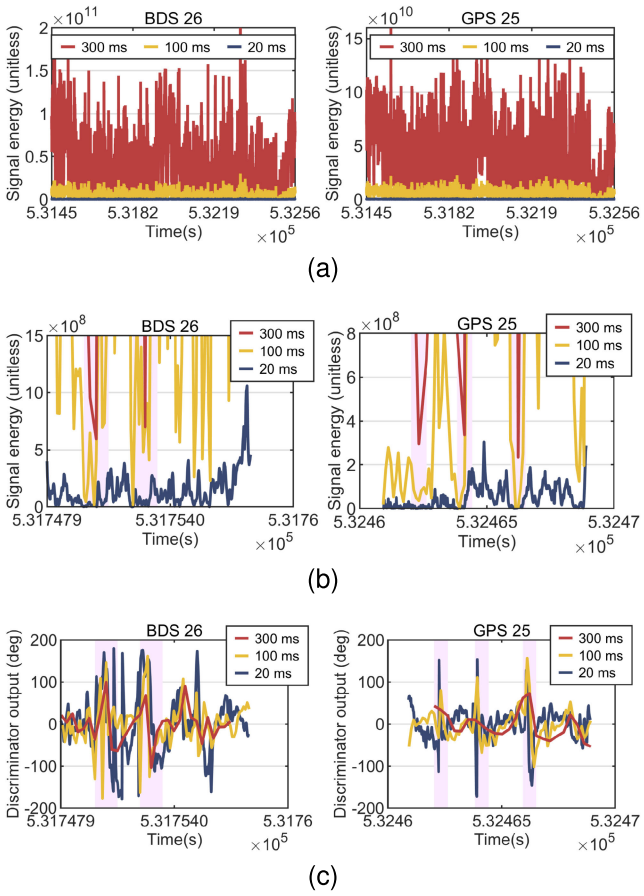

Fig. 13. Short-term signal blockage analysis. (a) The energy of the long coherent integration signals of BDS 26 and GPS 25 in the whole experiment. (b) The energy of the long coherent integration signals of BDS 26 and GPS 25 within a specific time segment when signal blockage occurred. (c)The corresponding discriminator output of BDS 26 and GPS 25 in the segments of (b).

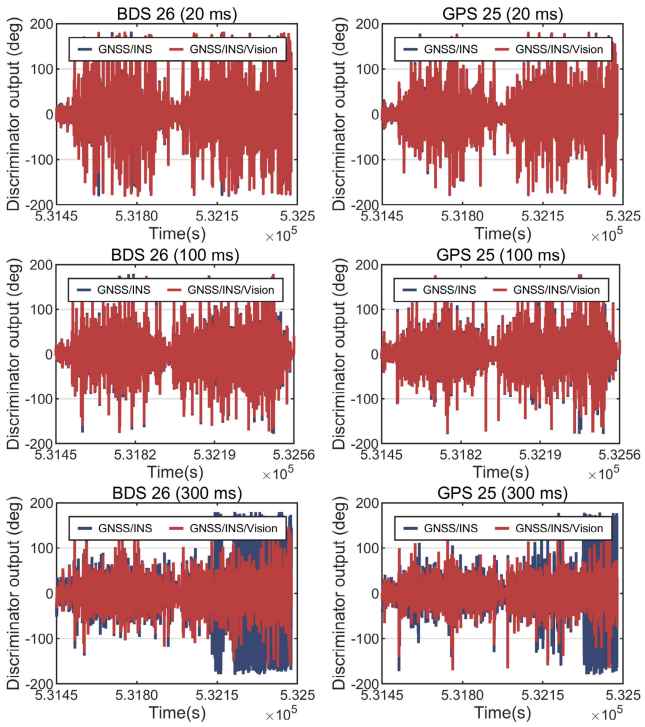

Fig. 14. The discriminator output comparison between the GNSS/INS and GNSS/INS/Vision ultra-tight integration of different coherent integration periods.

these satellites. Satellites with higher elevation angels, such as GPS 10, BDS 16, cause subtler dynamic stresses for the tracking loops, and they are more unlikely to be blocked by surrounding obstacles, so the noise of these satellites is lower. Although the multi-sensor ultra-tight integration has been adopted to eliminate the dynamic stress suffered by the tracking loop, corresponding dynamic residuals should also be tracked by it. Hence, satellites with lower elevation angles cause higher discriminator output noise.

Figure 13 shows the results of an analysis aimed at understanding how long coherent integration enhances tracking performance under frequent carrier phase signal blockages, such as those caused by tree branches and trunks in this typical scenario. Essentially, long coherent integration accumulates the signal energy, increasing the signal SNR. Figure 13a shows the signal energy of BDS 26 and GPS 25 of the entire experiment. The signal energy is evaluated by calculating the squared magnitude of the long coherent integration complex signal. Theoretically, the signal of N times of integration length has the energy scaled by N^2 without external interference, and the white thermal noise only increases by N times, which thus improves the signal SNR by N times. Since the processed IF signal is a quantized digital signal, the estimate of the signal energy is dimensionless. It is evident that the signal energy of long coherent integration is considerably higher than that of short term integration periods.

Several time segments exhibiting signal blockage are chosen from the Fig. 13a to meticulously analyze the impact of various coherent integration periods. The predetection signal energy of BDS 26 and GPS 25 within the selected analysis period is shown in Fig. 13b, and the corresponding discriminator output is shown in Fig. 13c. The occurrence of signal abnormality is highlighted by the light pink background. The results clearly show that a 300 ms integration period is sufficient to accumulate adequate signal energy, resulting in small phase discrimination errors. In contrast, the other two integration periods fail to maintain stable signal tracking. The corresponding phase discriminator output exhibits abrupt changes, leading to cycle slips. In the time domain, extended coherent integration time yields two benefits in addressing signal interference. On one hand, long coherent integration time increases the signal SNR, which improves the signal tracking sensitivity incredibly. On the other hand, when the signal is blocked for a very short term (dozens of milliseconds) by a tree trunk or telegraph pole, etc., it is still likely to cause cycle slips for short coherent integration periods. A coherent integration period exceeding the duration of the short blockage interval can still effectively accumulate energy, thereby ensuring continuous and stable tracking of interfered signals.

As mentioned before, the residual dynamic stresses remaining after ultra-tight compensation are tracked by the long coherent integration tracking loop. Therefore, the accuracy of the ultra-tight aiding information determines the achievable length of coherent integration. Figure 14 shows the results of

a test which was conducted to examine the influence of ultra-tight integration of GNSS/INS and GNSS/INS/Vision on the performance of long coherent integration tracking. The results include two representative satellites, GPS 25 and BDS 26. It is clearly illustrated that the GNSS/INS/Vision integration of the MUT-LCI architecture has the capability to provide the aiding information accurate enough to support much longer coherent integration time. When the integration period is 20 or 100 ms, the performances of the GNSS/INS and multi-sensor ultra-tight integration are comparable. However, as the integration period is 300 ms, the high dynamic residual errors of GNSS/INS will accumulate within the integration interval, causing serious loss of lock.

Since our research focuses on mitigating the dynamic stress caused by receiver–satellite relative motion through multi-sensor ultra-tightly coupled integration, an OCXO is adopted. A multichannel cooperative loop [38] can be employed to compensate for the receiver oscillator instability, enabling the use of a lower-grade oscillator to achieve a coherent integration time comparable to that of an OCXO. More details can be found in our previous work in [38].

In this section, we assessed the performance of the MUT-LCI architecture in signal tracking. The ultra-tight integration of GNSS/INS/Vision is essential to provide accurate loop aiding information, enabling the coherent integration periods long enough to track GNSS signals in extreme harsh environments.

B. GNSS Carrier Phase Measuring Performance

The performance of the MUT-LCI architecture is assessed at the carrier phase observation level, in which the errors of the carrier phase measurements of the standalone GNSS, ultra-tightly coupled GNSS/INS LCI and MUT-LCI are compared to verify the superiority of the MUT-LCI tracking.

The carrier phase errors are derived by three times of difference operations [54]. It is a transformed GNSS triple difference method designed for the evaluation of GNSS observation errors. First, the satellite-receiver distance in the LOS direction is calculated using the receiver's position from the ground truth system, and the difference between the carrier phase observation and the absolute satellite-receiver range is carried out. Second, a satellite with strong signal strength is selected as the reference satellite, and the difference between the first difference result of the reference satellite and that of other satellites is conducted, eliminating the receiver clock error term. Finally, the difference of the first two-step difference results over two successive epochs is computed. Since the interval between two successive epochs is 1 second in our experiment, the slow-varying error sources, including the atmospheric delays, satellite clock errors, and the antenna phase center errors, can be determined as ignorable after the third difference. As a result, only the cycle slips and modulated white noise are left, which are shown in Fig. 15.

The observations of the standalone GNSS were generated by the commercial GNSS receiver module, ublox-F9P. The GNSS/INS LCI 100 ms configuration refers to the ultra-tightly coupled GNSS/INS integration system with a 100 ms coherent integration time and a 1 Hz PLL bandwidth, which reflects the most advanced performance the dual-sensor integration can

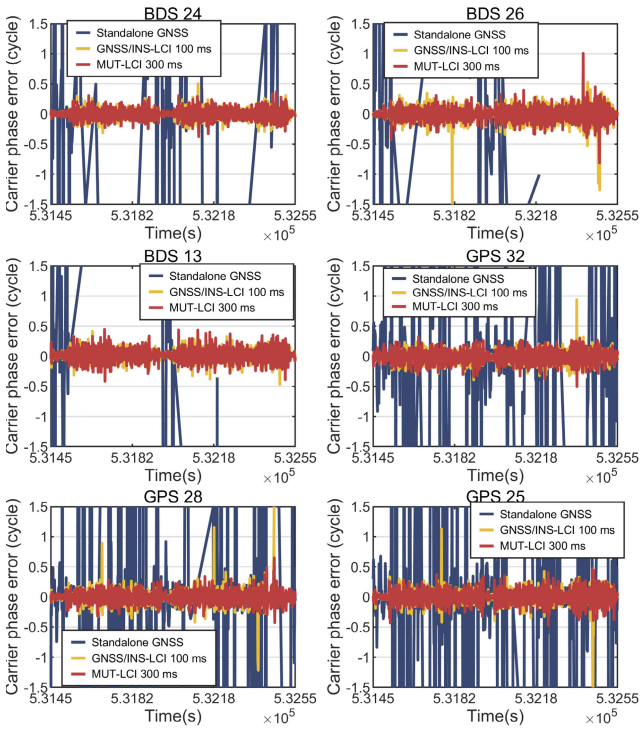

Fig. 15. The carrier phase observation errors of standalone GNSS (ublox-F9P), GNSS/INS-LCI 100 ms and MUT-LCI 300 ms.

provide. More details can be found in our previous work in [54]. Our proposed MUT-LCI architecture conducted a coherent integration period of 300 ms. The loop bandwidth should be as narrow as possible to suppress thermal noise, while still wide enough to track residual dynamics, atmospheric delays, clock drifts, and other variations. In the MUT-LCI architecture employing a 300 ms coherent integration time, the PLL bandwidth was set to 0.6 Hz.

Three representative BDS and GPS satellites' results are displayed. It is obvious that the standalone GNSS receiver outputs carrier phase observations with extreme frequent cycle slips. Ublox-F9P is a state-of-art multi-band GNSS receiver aiming at delivering centimeter level accuracy for autonomous mobile robots, etc. This indicates that a standalone receiver is unable to track GNSS carrier signals accurately in extreme harsh environments. On the contrary, the other two ultra-tightly coupled LCI techniques present carrier phase observations with satisfying accuracy. Besides, frequent half-cycle slips are observed in the standalone GNSS carrier phase observations, but the GNSS/INS-LCI 100 ms and MUT-LCI 300 ms seldom produce half-cycle slips due to the adoption of the four-quadrant carrier phase discriminator. The GNSS/INS-LCI 100 ms, however, still generates some cycle slips larger than a half cycle, leading to the deterioration of positioning accuracy, whereas the MUT-LCI exhibits minimal cycle slips.

In order to assess the continuity of the carrier phase observations, we performed a missing data detection, and the corresponding results are shown in Fig. 16. The missing data detection was conducted by calculating the difference of two successive carrier phase time stamps. As the carrier phase output frequency was set as 1 Hz, the detection values of more than 1 second would indicate the occurrence of data

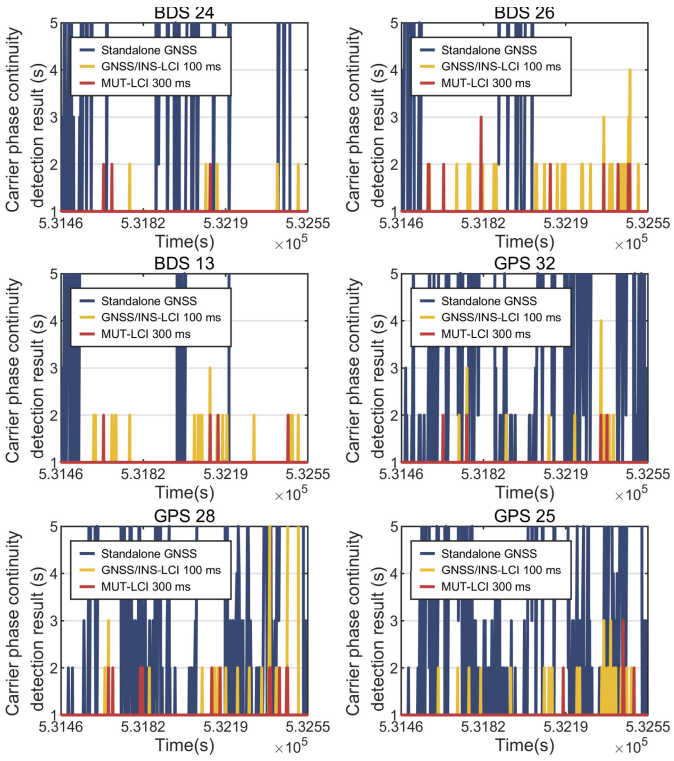

Fig. 16. The carrier phase missing data detection results of standalone GNSS (ublox-F9P), GNSS/INS-LCI 100 ms and MUT-LCI 300 ms.

missing. The standalone GNSS exhibits the poorest carrier phase continuity. It is noted that the three standalone GNSS BDS satellites depicted exhibit periods of missing data ranging from dozens to even hundreds of seconds. However, as the y-axis was limited to below 5 seconds for clarity in the demonstration, the corresponding curves of the standalone GNSS BDS satellites are not seen in Fig. 16. The poor availability of the standalone GNSS significantly limits high-precision positioning capabilities, especially in challenging environments. Although the GNSS/INS-LCI 100 ms enhances carrier phase continuity to some extent, it still experiences frequent data dropouts, resulting in degradation of positioning performance. The MUT-LCI 300 ms, however, demonstrates few data dropouts, indicating the best carrier phase availability and continuity. In summary, long coherent integration tracking is capable of improving the carrier phase accuracy and continuity radically. Multi-sensor ultra-tight integration serves as the cornerstone, enabling the adequate extension of coherent integration periods to ensure accurate and continuous carrier phase measurements in extreme harsh environments. The MUT-LCI 300 ms is capable of generating carrier phase observations with the best accuracy and continuity, thereby ensuring high performance for the RTK positioning algorithm.

C. Positioning Accuracy Evaluation

In this section, the positioning accuracy of the MUT-LCI architecture is evaluated in detail. Both the RTK and overall integrated navigation positioning results will be analyzed.

Following the experiment of the previous subsection, the observations of the standalone GNSS receiver (u-blox F9P), GNSS/INS-LCI 100 ms and MTU-LCI 300 ms are sent to the robot's RTK positioning module for processing, comparing the carrier phase performance of the three methods at the RTK positioning level. The core of the RTK algorithm is PLANSoft [55], a multi-constellation dual-frequency RTK software developed by Position, Location And Navigation (PLAN) Group, the university of Calgary. In this experiment, the observations of GPS L1 and BDS B1I were used in the RTK algorithm, and the carrier phase ambiguity resolution was turned on. The RTK baseline length is approximately 3 kilometers.

TABLE I

RTK POSITIONING ERROR STATISTICS OF THE STANDALONE GNSS, GNSS/INS-LCI 100 MS AND MUT-LCI 300 MS

	Configuration	Max (m)	RMS (m)	Cep95 (m)
North	Standalone GNSS	7.308	2.468	4.244
	GNSS/INS-LCI 100 ms	0.564	0.176	0.413
	MUT-LCI 300 ms	**0.145**	**0.030**	**0.066**
East	Standalone GNSS	3.971	1.141	2.492
	GNSS/INS-LCI 100 ms	0.897	0.228	0.591
	MUT-LCI 300 ms	**0.169**	**0.026**	**0.054**
Down	Standalone GNSS	25.628	7.359	13.276
	GNSS/INS-LCI 100 ms	2.729	0.664	1.818
	MUT-LCI 300 ms	**0.400**	**0.076**	**0.150**

The overall RTK positioning errors in the north, east and vertical directions are shown in Fig. 17. It is evident that the RTK positioning errors of the standalone GNSS are remarkably larger than that of the other two techniques. The RTK ambiguity fixing rates, measured since system initialization, for these three configurations are 7.6%, 81.3% and 100.0%. Although the GNSS/INS-LCI 100 ms provides high-precision positioning results most of the time, there are two segments during which the accuracy deteriorates. The MUT-LCI 300 ms can maintain continuous and accurate carrier signal tracking, thereby generating robust carrier phase observations, which ensures the consistent fixing of the carrier phase ambiguity.

The statistics of the RTK positioning errors are shown in Table. I. The Root Mean Square (RMS) values of the positioning errors in the standalone GNSS, GNSS/INS-LCI 100 ms and MUT-LCI 300 ms are 2.468 m, 0.176 m and 0.03 m in the north direction, respectively; and the east RMS values are 1.141 m, 0.228 m, 0.026 m, respectively. The results of the Standalone GNSS solution were obtained by processing the u-blox F9P observations in RTK mode using PLANSoft. However, due to the poor carrier phase availability of the F9P receiver in harsh environments, the RTK algorithm failed to produce fixed solutions, resulting in meter-level positioning accuracy. The positioning of the GNSS/INS-LCI 100 ms is accurate to the decimeter level. The best positioning outcome is provided by the MUT-LCI architecture with a coherent integration period of 300 ms. Both the ambiguity fixing rate and positioning error RMS demonstrate a solid centimeter level accuracy. Moreover, the 95% circular error probable (CEP 95) is evaluated. The CEP 95 values of the standalone GNSS, GNSS/INS-LCI 100 ms and MUT-LCI 300 ms horizontal positioning errors are 4.496 m, 0.732 m and 0.081 m. respectively. This indicates that the MUT-LCI 300 ms yields positioning results where 95% of the horizontal errors are below 0.081 m, fulfilling the rigorous demands for

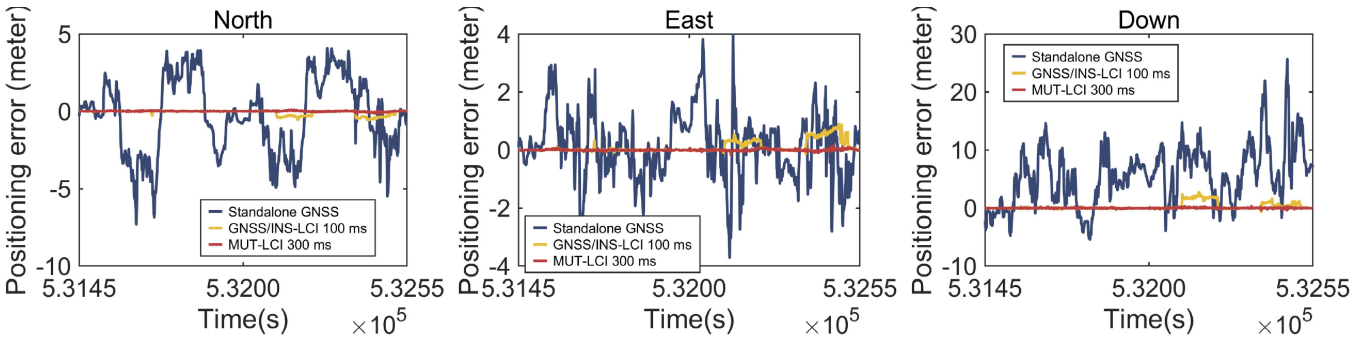

Fig. 17. The overall RTK positioning errors of the standalone GNSS (ublox-F9P), GNSS/INS-LCI 100 ms and MUT-LCI 300 ms in the north, east and vertical direction.

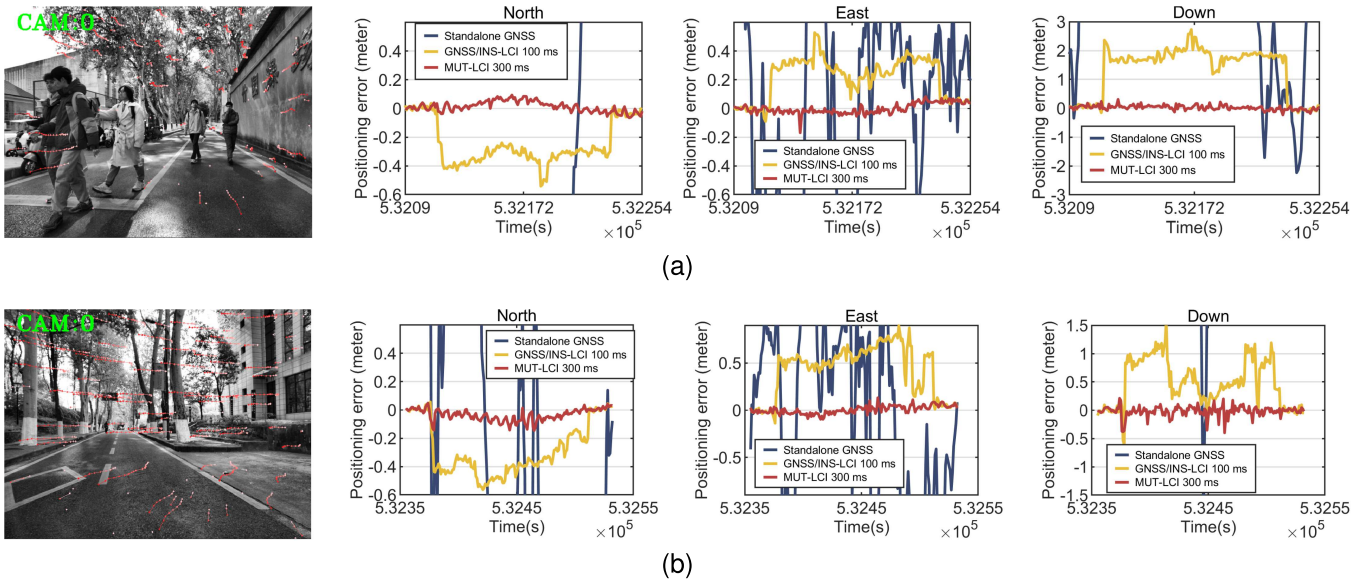

Fig. 18. The three-dimensional RTK positioning errors of typical GNSS challenging scenarios, and the real scene is shown in the leftmost figure (a) Signal blockage scenario (b) Severe multipath scenario.

high-precision robot navigation. Since only the satellites above the horizon can be tracked by the GNSS receivers, the vertical solution is less precise than the horizontal solution. The RMS values of the vertical positioning errors of the standalone GNSS, GNSS/INS-LCI and MUT-LCI are 7.359 m, 0.664 m and 0.076 m, respectively. The overall positioning error analysis indicates that the proposed MUT-LCI architecture has the capability to provide three-dimensional centimeter level positioning solution in extreme harsh environments.

As mentioned earlier, there are two time segments where the errors of the GNSS/INS-LCI 100 ms increases noticeably. Pronounced drops and more severe fluctuations in C/N_0 can also be observed in these segments (shown in Fig. 11). The real scenes from the camera data and corresponding RTK positioning errors of the two segments are shown in Fig. 18a and 18b in detail, respectively. In the first segment, except for the dense foliage, the robot passed by a concrete wall which blocked the GNSS signals, disrupting the continuity of carrier phase observations. Additionally, signal blockages were frequently encountered due to the presence of pedestrians in the vicinity, which is a common scenario for autonomous vehicles. Such complex signal conditions made the GNSS/INS-LCI 100 ms fail to track carrier phase signals stably, causing frequent loss of lock and discontinuity of the carrier phase observations, as depicted in the corresponding time segments in Fig. 16. As a result, the GNSS/INS-LCI 100 ms could not resolve the carrier phase ambiguity, thereby producing positioning errors of several decimeters. The MUT-LCI 300 ms, however, demonstrated consistent centimeter level positioning accuracy, showing the superior performance in the resistance of signal blockages. The second segment is a scenario that the robot passed a road where a heavy tree canopy lied above and a tall building with abundant glass windows stood on the right side. It is a typical complex scene where the received GNSS signals are a combination of various LOS, weakened and multipath components. As can be seen in Fig. 11, the significant drop and more intense variations of C/N_0 measurements in this segment (532350–532550s) indicates more severe multipath interference. Even in this scenario, the MUT-LCI 300 ms could still track the carrier signals accurately (shown in Fig. 12) and present robust carrier phase observations without cycle slips (shown in Fig. 15). Hence the corresponding positioning solution is centimeter accurate. The test results of the two typical scenarios proves that the MUT-LCI has high performances in term of blockage resistance and multipath mitigation, addressing

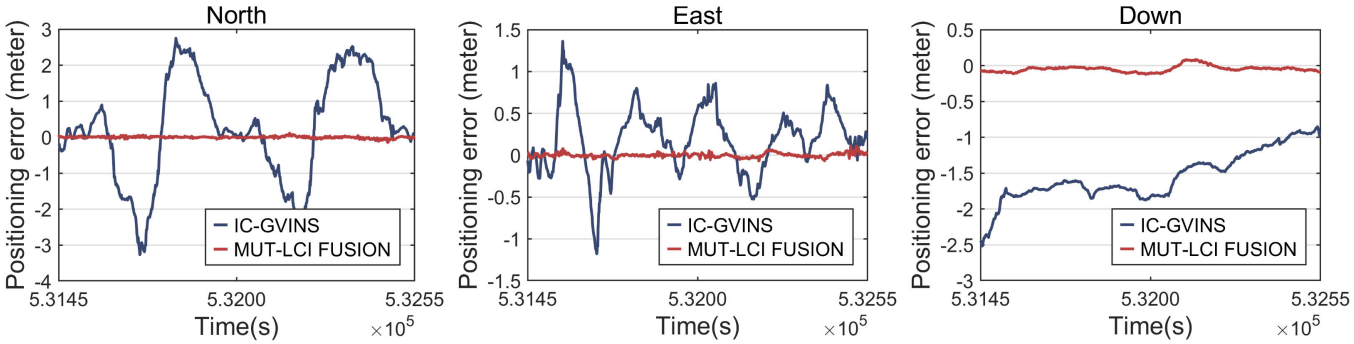

Fig. 19. Ultimate integrated positioning errors of the IC-GVINS and MUT-LCI 300 ms.

TABLE II
ULTIMATE INTEGRATED POSITIONING ERROR STATISTICS OF THE IC-GVINS AND MUT-LCI FUSION

	Configuration	Max (m)	RMS (m)	Cep95 (m)
North	IC-GVINS	3.264	1.462	2.451
	MUT-LCI Fusion	**0.147**	**0.029**	**0.061**
East	IC-GVINS	1.362	0.439	0.904
	MUT-LCI Fusion	**0.111**	**0.025**	**0.051**
Down	IC-GVINS	2.516	1.582	2.061
	MUT-LCI Fusion	**0.122**	**0.063**	**0.106**

the poor availability of the high-precision GNSS in complex environments.

As previously described, the MUT-LCI is a semi-tightly coupled Kalman Filter-based ultra-tight integration architecture. The result of the RTK positioning will be used in the MSCKF for the fusion with the IMU and camera data, generating the ultimate integrated navigation solution. In order to evaluate the comprehensive performance of the MUT-LCI, the ultimate integration navigation results of the MUT-LCI architecture are compared with that of another GNSS/INS/Vision semi-tightly coupled solution: IC-GVINS [21], an open source, real-time, INS-centric GNSS-Visual-Inertial navigation system. The u-blox F9P raw observations were processed by PLANSoft, generating the corresponding GNSS positioning results, which were then sent to the IC-GVINS system for the fusion with IMU and camera data. In terms of data types, this is consistent with the top-level data fusion algorithm used in our proposed MUT-LCI system. The key difference lies in our adoption of multi-sensor ultra-tightly coupled integration and long coherent integration carrier phase tracking. Figure 19 shows the comparison results, demonstrating a huge precision gap between the IC-GVINS and MUT-LCI system. Corresponding positioning error statistics are shown in Table. II. The RMS values of the north positioning errors in the IC-GVINS and MUT-LCI are 1.462 m and 0.029 m, respectively, and the east error RMS values are 0.439 m and 0.025 m, respectively. Since the GNSS is the only source to provide the absolute positioning constraint, its precision determines the absolute precision of the ultimate navigation solution to a large extent. The RMS values of the vertical positioning errors in the two sets are 1.582 m and 0.063m, respectively. It is noted that the curves of the vertical positioning errors vary slowly, which is due to the lack of vertical dynamic stimulation for a wheeled robot. As a result, the vertical positioning error curve of the IC-GVINS stays below 0 all the time.

In this subsection, the positioning accuracy of the MUT-LCI is evaluated in detail. The results indicate that the MUT-LCI architecture has high performances in term of resisting the GNSS signal blockage and mitigating the multipath effects, and it is fully capable of providing robust centimeter-level RTK positioning in harsh environments. Benefit from the superiority of the RTK positioning, the ultimate integrated navigation solution of the MUT-LCI shows a more robust centimeter level precision.

It is important to note that due to the highly challenging test environment, the ground truth system achieves sub-centimeter accuracy in some segments but is limited to centimeter-level accuracy in others. Consequently, the positioning error statistics may not be entirely precise. However, based on the positioning error statistics and RTK fixing rates, the MUT-LCI demonstrates positioning accuracy comparable to that of a high-precision POS system, typically at the centimeter level.

V. CONCLUSION

We have proposed an ultra-tightly coupled GNSS/INS/Vision long coherent integration receiver architecture that performs GNSS signal tracking, RTK positioning and multi-sensor integration for the high precision positioning of autonomous vehicles, such as self-driving cars and smart delivery robots. Unlike the conventional loosely or tightly coupled multi-sensor integration solutions, we turned the GNSS receiver into a “white box”, and utilized the superior dead reckoning ability of the visual-inertial navigation system to assist the tracking of the carrier phases. In order to improve the GNSS signal tracking performance radically, we implemented the long coherent integration PLL on the basis of the deepest level of multi-sensor integration. Besides, a four-quadrant phase error discriminator was adopted to increase the discrimination range, mitigating the cycle slips due to the instantaneous signal abnormality. The top-level RTK/INS/Vision integration is conducted with a MSCKF, which has low processing load and high accuracy.

We assessed the performance the of the proposed MUT-LCI architecture based on an intelligent transportation wheeled robot. Three different levels of tests were conducted, including the signal tracking, carrier phase observation and positioning. The MUT-LCI showed superior performances in terms of weak signal tracking, signal blockage resistance and multipath mitigation. The experimental results demonstrated that the

MUT-LCI architecture possesses the ability to track carrier signals accurately in extreme harsh environments, thereby providing robust three-dimensional centimeter accurate positioning.

Collectively, compared with other conventional multi-sensor positioning techniques, the proposed MUT-LCI achieved the best high-precision absolute positioning performance (continuous centimeter-level accuracy) in challenging environments under dense foliage and surrounded by buildings. Our work significantly improves GNSS availability, demonstrating the strong potential of GNSS to support high-precision positioning for autonomous vehicles in large-scale, unknown, and challenging environments. This, in turn, enhances the safety, efficiency, and autonomy of intelligent transportation systems. Future work will incorporate oscillator instability compensation techniques to enable lower-grade oscillators, such as Temperature Compensated Crystal Oscillators (TCXOs), to achieve satisfactory performance in long coherent integration (LCI) carrier phase tracking. Moreover, the perception ability of the camera will be utilized to sense the GNSS signal conditions, thereby generating an environment-oriented adaptive tracking strategy.

ACKNOWLEDGMENT

The algorithm is implemented by the Integrated and Intelligent Navigation (I2Nav) Group, GNSS Research Center, Wuhan University. Xin Feng, Tisheng Zhang, Liqiang Wang, and Xiaoji Niu thank Mohamed Bochkati and Thomas Pany, who are with the Universität der Bundeswehr München.

REFERENCES

[1] T. E. Humphreys, M. J. Murrian, and L. Narula, "Deep-urban unaided precise global navigation satellite system vehicle positioning," *IEEE Intell. Transp. Syst. Mag.*, vol. 12, no. 3, pp. 109–122, Fall. 2020.

[2] Z. Xiao, J. Shu, H. Jiang, G. Min, H. Chen, and Z. Han, "Perception task offloading with collaborative computation for autonomous driving," *IEEE J. Sel. Areas Commun.*, vol. 41, no. 2, pp. 457–473, Feb. 2023.

[3] S. Zhao, Y. Chen, and J. A. Farrell, "High-precision vehicle navigation in urban environments using an MEM's IMU and single-frequency GPS receiver," *IEEE Trans. Intell. Transp. Syst.*, vol. 17, no. 10, pp. 2854–2867, Oct. 2016.

[4] Z. Xiao, Y. Chen, M. Alazab, and H. Chen, "Trajectory data acquisition via private car positioning based on tightly-coupled GPS/OBD integration in urban environments," *IEEE Trans. Intell. Transp. Syst.*, vol. 23, no. 7, pp. 9680–9691, Jul. 2022.

[5] E. D. Kaplan and C. Hegarty, *Understanding GPS/GNSS: Principles and Applications*. Norwood, MA, USA: Artech House, 2017.

[6] V. Havyarimana, Z. Xiao, T. Semong, J. Bai, H. Chen, and L. Jiao, "Achieving reliable intervehicle positioning based on redheffer weighted least squares model under multi-GNSS outages," *IEEE Trans. Cybern.*, vol. 53, no. 2, pp. 1039–1050, Feb. 2023.

[7] J. Xiao et al., "Vehicle trajectory interpolation based on ensemble transfer regression," *IEEE Trans. Intell. Transp. Syst.*, vol. 23, no. 7, pp. 7680–7691, Jul. 2022.

[8] G. MacGougan, G. Lachapelle, R. Nayak, and A. Wang, "Overview of GNSS signal degradation phenomena," in *Proc. Int. Symp. Kinematic Syst. Geodesy, Geomatics Navigat.*, 2001, pp. 87–100.

[9] Q. Wang, F. Cheng, and T. Zhang, "5G impacts analysis on the beidou RDSS system in 2.5 GHz band," *GPS Solutions*, vol. 27, no. 1, p.24, Jan. 2023.

[10] A. Parkins, "Increasing GNSS RTK availability with a new single-epoch batch partial ambiguity resolution algorithm," *GPS Solutions*, vol. 15, no. 4, pp. 391–402, Oct. 2011.

[11] R. Tu, M. Ge, H. Zhang, and G. Huang, "The realization and convergence analysis of combined PPP based on raw observation," *Adv. Space Res.*, vol. 52, no. 1, pp. 211–221, Jul. 2013.

[12] X. Li et al., "Review of PPP–RTK: Achievements, challenges, and opportunities," *Satell. Navigat.*, vol. 3, no. 1, p.28, Dec. 2022.

[13] W. Feng, Y. Zhao, L. Zhou, D. Huang, and A. Hassan, "Fast cycle slip determination for high-rate multi-GNSS RTK using modified geometry-free phase combination," *GPS Solutions*, vol. 24, no. 2, pp. 1–11, Apr. 2020.

[14] X. Li et al., "Accuracy and reliability of multi-GNSS real-time precise positioning: GPS, GLONASS, BeiDou, and Galileo," *J. Geodesy*, vol. 89, no. 6, pp. 607–635, Jun. 2015.

[15] S. Pan, X. Meng, W. Gao, S. Wang, and A. Dodson, "A new approach for optimising GNSS positioning performance in harsh observation environments," *J. Navigat.*, vol. 67, no. 6, pp. 1029–1048, Nov. 2014.

[16] G. Falco, M. Pini, and G. Marucco, "Loose and tight GNSS/INS integrations: Comparison of performance assessed in real urban scenarios," *Sensors*, vol. 17, no. 2, p. 255, Jan. 2017.

[17] V. Havyarimana, Z. Xiao, A. Sibomana, D. Wu, and J. Bai, "A fusion framework based on sparse Gaussian–Wigner prediction for vehicle localization using GDOP of GPS satellites," *IEEE Trans. Intell. Transp. Syst.*, vol. 21, no. 2, pp. 680–689, Feb. 2020.

[18] S. Han and J. Wang, "Integrated GPS/INS navigation system with dual-rate Kalman filter," *GPS Solutions*, vol. 16, no. 3, pp. 389–404, Jul. 2012.

[19] D. A. Grejner-Brzezinska, C. K. Toth, T. Moore, J. F. Raquet, M. M. Miller, and A. Kealy, "Multisensor navigation systems: A remedy for GNSS vulnerabilities?," *Proc. IEEE*, vol. 104, no. 6, pp. 1339–1353, Jun. 2016.

[20] R. Mur-Artal and J. D. Tardós, "Visual-inertial monocular SLAM with map reuse," *IEEE Robot. Autom. Lett.*, vol. 2, no. 2, pp. 796–803, Apr. 2017.

[21] X. Niu, H. Tang, T. Zhang, J. Fan, and J. Liu, "IC-GVINS: A robust, real-time, INS-centric GNSS-visual-inertial navigation system," *IEEE Robot. Autom. Lett.*, vol. 8, no. 1, pp. 216–223, Jan. 2023.

[22] K.-W. Chiang, D. T. Le, K.-Y. Lin, and M.-L. Tsai, "Multifusion schemes of INS/GNSS/GCPs/V-SLAM applied using data from smartphone sensors for land vehicular navigation applications," *Inf. Fusion*, vol. 89, pp. 305–319, Jan. 2023.

[23] M. Lv, H. Wei, X. Fu, W. Wang, and D. Zhou, "A loosely coupled extended Kalman filter algorithm for agricultural scene-based multi-sensor fusion," *Frontiers Plant Sci.*, vol. 13, pp. 849260, Apr. 2022.

[24] S. Cao, X. Lu, and S. Shen, "GVINS: Tightly coupled GNSS–visual–inertial fusion for smooth and consistent state estimation," *IEEE Trans. Robot.*, vol. 38, no. 4, pp. 2004–2021, Aug. 2022.

[25] Z. Gao, M. Ge, Y. Li, Y. Pan, Q. Chen, and H. Zhang, "Modeling of multi-sensor tightly aided BDS triple-frequency precise point positioning and initial assessments," *Inf. Fusion*, vol. 55, pp. 184–198, Mar. 2020.

[26] Y. Deng, Y. Shan, Z. Gong, and L. Chen, "Large-scale navigation method for autonomous mobile robot based on fusion of GPS and LiDAR SLAM," in *Proc. Chin. Autom. Congr. (CAC)*, Nov. 2018, pp. 3145–3148.

[27] X. Li, X. Wang, J. Liao, X. Li, S. Li, and H. Lyu, "Semi-tightly coupled integration of multi-GNSS PPP and S-VINS for precise positioning in GNSS-challenged environments," *Satell. Navigat.*, vol. 2, no. 1, pp. 1–14, Dec. 2021.

[28] X. Li, Z. Qin, Z. Shen, X. Li, Y. Zhou, and B. Song, "A high-precision vehicle navigation system based on tightly coupled PPP-RTK/INS/odometer integration," *IEEE Trans. Intell. Transp. Syst.*, vol. 24, no. 2, pp. 1855–1866, Feb. 2023.

[29] Q. Xu, Z. Gao, J. Lv, C. Yang, and Y. Li, "Multi-sensor and analytical constraints tightly augmented BDS-3 RTK for vehicle-borne positioning," *IEEE Trans. Intell. Transp. Syst.*, vol. 24, no. 10, pp. 11132–11145, Oct. 2023.

[30] J. E. Yoder and T. E. Humphreys, "Low-cost inertial aiding for deep-urban tightly coupled multi-antenna precise GNSS," *Navigation, J. Inst. Navigat.*, vol. 70, no. 1, 2023, Art. no. navi.561.

[31] F. Wang and J. Geng, "GNSS PPP-RTK tightly coupled with low-cost visual-inertial odometry aiming at urban canyons," *J. Geodesy*, vol. 97, no. 7, p.66, Jul. 2023.

[32] S. Li, X. Li, H. Wang, Y. Zhou, and Z. Shen, "Multi-GNSS PPP/INS/vision/LiDAR tightly integrated system for precise navigation in urban environments," *Inf. Fusion*, vol. 90, pp. 218–232, Feb. 2023.

[33] T. Zhang, J. Shi, T. Lin, X. Feng, and X. Niu, "GNSS position-aided delay-locked loops for accurate urban navigation," *GPS Solutions*, vol. 27, no. 3, p.127, Jul. 2023.

[34] S. Zhao and D. Akos, "An open source GPS/GNSS vector tracking loop-implementation, filter tuning, and results," in *Proc. Int. Tech. Meeting Inst. Navigat.*, 2011, pp. 1293–1305.

[35] S. M. Martin, "Performance analysis of a RTK vector phase-locked loop architecture for GPS signal tracking in degraded environments," *Navigation, J. Inst. Navigat.*, vol. 70, no. 4, 2023, Art. no. navi.626.
[36] S. Kennedy and J. Rossi, "Performance of a deeply coupled commercial grade GPS/INS system from KVH and NovAtel Inc.," in *Proc. IEEE/ION Position, Location Navigat. Symp.*, May 2008, pp. 17–24.
[37] Y. Ban, X. Niu, T. Zhang, Q. Zhang, and J. Liu, "Modeling and quantitative analysis of GNSS/INS deep integration tracking loops in high dynamics," *Micromachines*, vol. 8, no. 9, p. 272, Sep. 2017.
[38] X. Feng, T. Zhang, X. Niu, T. Pany, and J. Liu, "Improving GNSS carrier phase tracking using a long coherent integration architecture," *GPS Solutions*, vol. 27, no. 1, p.37, Jan. 2023.
[39] A. Soloviev, C. Toth, and D. Grejner-Brzezinska, "Performance of deeply integrated GPS/INS in dense forestry areas," *J. Appl. Geodesy*, vol. 6, no. 1, pp. 3–13, Jan. 2012.
[40] T. Pany, "Coherent integration time: The longer, the better," *Inside GNSS*, vol. 4, pp. 52–61, Nov. 2009.
[41] T. Ren and M. G. Petovello, "A stand-alone approach for high-sensitivity GNSS receivers in signal-challenged environment," *IEEE Trans. Aerosp. Electron. Syst.*, vol. 53, no. 5, pp. 2438–2448, Oct. 2017.
[42] F. Van Diggelen, *A-GPS: Assisted GPS, GNSS, and SBAS*. Norwood, MA, USA: Artech House, 2009.
[43] T. Fan, T. Zhang, H. Zhang, J. Mo, and X. Niu, "A double sideband combined tracking method for Galileo E5 AltBOC signals," *Satell. Navigat.*, vol. 4, no. 1, p.27, Dec. 2023.
[44] Z. Zuo, B. Yang, Z. Li, and T. Zhang, "A GNSS/IMU/vision ultra-tightly integrated navigation system for low altitude aircraft," *IEEE Sensors J.*, vol. 22, no. 12, pp. 11857–11864, Jun. 2022.
[45] B. Priot, C. Peillon, V. Calmettes, and M. Sahmoudi, "Performance assessment of an ultra-tightly coupled vision-aided INS/GNSS navigation system," in *Proc. Int. Tech. Meeting Inst. Navigat.*, pp. 652–661.
[46] A. Fernández et al., "ATENEA: Advanced techniques for deeply integrated GNSS/INS/LiDAR navigation," in *Proc. 5th ESA Workshop Satell. Navigat. Technol. Eur. Workshop GNSS Signals Signal Process. (NAVITEC)*, Dec. 2010, pp. 1–8.
[47] A. I. Mourikis and S. I. Roumeliotis, "A multi-state constraint Kalman filter for vision-aided inertial navigation," in *Proc. IEEE Int. Conf. Robot. Autom.*, Apr. 2007, pp. 3565–3572.
[48] G. Gao and G. Lachapelle, "INS-assisted high sensitivity GPS receivers for degraded signal navigation," in *Proc. 19th Int. Tech. Meeting Satell. Division Inst. Navigat. (ION GNSS)*, 2018, pp. 2977–2989.
[49] E. Shin, "Estimation techniques for low-cost inertial navigation," Univ. Calgary, Calgary, AB, Canada, 2005.
[50] T. Zhang, Y. Ban, X. Niu, W. Guo, and J. Liu, "Improving the design of MEMS INS-aided PLLs for GNSS carrier phase measurement under high dynamics," *Micromachines*, vol. 8, no. 5, p. 135, Apr. 2017.
[51] *Spirent GSS6450 Multi-Frequency Record & Playback System*, Spirent, Crawley, U.K., 2023.
[52] *ZED-F9P-04B High Precision GNSS Module Professional Grade*, U-blox, Thalwil, Switzerland, 2023.
[53] D. Hai, C. L. Tsang, G. Zhang, and L.-T. Hsu, "GNSS measurement performance in vegetation environments: Assessment and analysis in signal processing level," in *Proc. ION GNSS, Int. Tech. Meeting Satell. Division Inst. Navigat.*, Oct. 2024, pp. 1939–1951.
[54] T. Zhang, X. Feng, X. Niu, M. Bochkati, T. Pany, and J. Liu, "GNSS carrier phase improvement using a MEMS INS-aided long coherent architecture for high precision navigation," *IEEE Trans. Intell. Transp. Syst.*, vol. 25, no. 11, pp. 16745–16760, Nov. 2024.
[55] R. Ong, "Reliability of combined GPS/GLONASS ambiguity resolution," *Masters Abstr. Int.*, vol. 49, no. 3, p. 4, 2018.

Xin Feng received the B.E. and M.E. degrees from Wuhan University, Wuhan, China, in 2018 and 2021, respectively, where he is currently pursuing the Ph.D. degree in geodesy and survey engineering with the School of Geodesy and Geomatics. His primary research interests include GNSS receiver and multi-sensor ultra-tightly integration.

Tisheng Zhang (Member, IEEE) received the B.Sc. and Ph.D. degrees in communication and information system from Wuhan University, Wuhan, China, in 2008 and 2013, respectively. From 2018 to 2019, he was a Post-Doctoral Researcher at The Hong Kong Polytechnic University. He is a Professor at the GNSS Research Center, Wuhan University. His research interests focus on the fields of GNSS receiver, multi-sensor deep integration, and robot navigation.

Liqiang Wang (Graduate Student Member, IEEE) received the B.E. and M.E. degrees from Wuhan University, China, in 2020 and 2023, respectively, where he is currently pursuing the Ph.D. degree with the GNSS Research Center. His primary research interests include GNSS/INS integrations, visual SLAM, and multi-sensor fusion navigation systems.

Xiaoji Niu (Member, IEEE) is currently a Professor with the GNSS Research Center, Wuhan University, China. He has published more than 90 academic papers and owns 28 patents. He leads a multi-sensor navigation group focusing on GNSS/INS integration, low-cost navigation sensor fusion, and its new applications.

Mohamed Bochkati received the bachelor's and master's degrees in geodesy and geoinformation from Technical University Munich. He is a Research Associate at the Institute of Space Technology and Space Applications (ISTA), Universität der Bundeswehr München. His research focuses on deeply coupled GNSS/INS integration and novel calibration techniques for MEMS-IMUs.

Thomas Pany (Senior Member, IEEE) is a Full Professor at the Faculty of Aerospace Engineering, Universität der Bundeswehr München, where he teaches satellite navigation. He focuses on GNSS/LTE/5G signal design and processing, software receivers, and GNSS/INS/LiDAR fusion. He has around 200 publications, including patents and one monograph.

Jingnan Liu is a member of Chinese Academy of Engineering, a Professor, and a Ph.D. Supervisor. He is an expert in geodesy and surveying engineering with a specialty in GNSS technology and applications. He has been engaged in the research of geodetic theories and applications, including national coordinate system establishment, GNSS technology and software development, and large project implementation.